Modeling Buildability in 3D Concrete Printing: A Discontinuous Galerkin Method with Cohesive Interfaces

Abdallah Kamhawi[a,*], Mania Aghaei Meibodi[a], Jesse Capecelatro[b,c]

[a] *Taubman College of Architecture and Urban Planning, University of Michigan, Ann Arbor, MI 48109, USA*

[b] *Department of Aerospace Engineering, University of Michigan, Ann Arbor, MI 48109, USA*

[c] *Department of Mechanical Engineering, University of Michigan, Ann Arbor, MI 48109, USA*

Abstract

Buildability, defined as the ability of a 3D concrete printed structure to sustain its own weight and maintain geometric stability, depends on both the evolving bulk material response and the integrity of interlayer bonds. Existing part-level simulation frameworks are typically based on continuous Galerkin formulations, which enforce displacement continuity across element boundaries and therefore cannot represent interlayer delamination. This paper presents a discontinuous Galerkin finite element method for simulating buildability in 3D concrete printing. The presented method captures both bulk plastic collapse and interlayer delamination in a unified framework. Interior facets are classified as either intra-layer or inter-layer. Intra-layer facets are coupled through symmetric interior penalty terms to recover bonded continuum behavior, whereas inter-layer facets are governed by a mixed-mode cohesive traction–separation law with structuration-dependent bond quality. The framework is further coupled to a time-dependent elasto-viscoplastic bulk model derived from rheological inputs and to a smooth element-activation scheme that represents progressive material deposition while maintaining a fixed computational mesh. The implementation is verified through six benchmark tests, demonstrating machine-precision accuracy where expected and optimal convergence for the full discretization. Validation against two experimental cases, a printed hollow cylinder failing by plastic collapse and a printed barrel vault failing by interlayer delamination, demonstrates that the dual-interface treatment activates the correct governing failure mode directly from the stress and damage fields, without a priori specification.

Keywords:
3D concrete printing, Buildability, Discontinuous Galerkin method, Cohesive zone model, Time-dependent mechanics

1. Introduction

3D Concrete Printing (3DCP) is a method of construction where a cement-based mortar is pumped and precisely deposited by a 3D printing nozzle mounted on a gantry system or a robotic arm [1–3]. Of most relevance to this paper is the technology's ability to manufacture bespoke, materially optimized structural elements such as vaults, and topology-optimized building elements (Figure 1) without incurring the additional time and costs of conventional formwork [4–10]. The structural performance gains enabled by these complex forms, however, are contingent on the ability to fabricate them reliably; the geometries required for structurally efficient designs often involve overhangs, cantilevers, and non-planar deposition paths that push the freshly printed material to the limits of its load-bearing capacity during construction [4].

Currently, the feasibility of a given geometry and print strategy is typically assessed through physical trial and error, where prototypes are printed, failures are observed, and a human expert adjusts the parameters iteratively [11, 12]. This approach is costly in both material and time, and it produces knowledge that is difficult to generalize beyond the specific geometry and material system tested. Computational models offer an alternative; by simulating the mechanical response of the printed structure during construction, including progressive material deposition, evolving fresh-state mechanical properties, and interlayer interactions, such models can identify likely failure conditions and governing failure modes before a physical print is attempted [13–17]. Reliable simulation tools for 3DCP are therefore a prerequisite for moving the field from empirical prototyping toward computationally-guided design and so-called "first-time right manufacturing."

Computational models for 3DCP span two scales [3, 18]. Process-level models address the mechanics of extrusion, including material flow through the nozzle and filament shape upon deposition, and are concerned with the local quality of the deposited bead [19–22]. Part-level models address the structural response of the entire deposited geometry during printing. These models assess whether the accumulating self-weight causes excessive deformation, yielding, buckling, or collapse [13–15, 17]. This paper is concerned exclusively with part-level modeling.

The central question that part-level simulations address is buildability, defined as the capacity of a printed structure to sustain its own weight and maintain dimensional stability throughout the 3DCP process, before the material has fully hardened [3, 4].

*Corresponding author.
Email address: `kamhawi@umich.edu` (Abdallah Kamhawi)

Buildability is distinct from the long-term structural capacity of the finished element; rather, it is a process-governed property associated with the printing stage, during which the material transitions from a soft paste to a load-bearing solid and the geometry grows incrementally with each deposited layer.

The majority of existing part-level buildability models assume horizontal layer deposition, where layers are stacked perpendicular to the gravity vector [13, 14, 17, 23–25]. In this configuration, self-weight acts normal to the layer interfaces, compressing successive layers together rather than pulling them apart (see Figure 1). Interlayer bonds are rarely challenged, and the dominant failure modes are elastic buckling [14, 26] and plastic collapse [26–28]. The structure either becomes geometrically unstable under compressive loading or the accumulated self-weight exceeds the material's evolving yield capacity.

Because buckling and plastic collapse are bulk phenomena, arising from geometric instability or material yielding within the deposited volume, existing models treat the printed structure as a continuous solid. The standard approach employs continuous Galerkin (CG) finite element methods [13, 17, 29], where adjacent elements share nodes along their common boundaries and the displacement field is continuous across every element interface by construction. This continuity assumption is valid when interlayer separation does not occur or is not the governing failure mode. Several groups have developed CG-based buildability models: Wolfs et al. [13] modeled the printed cylinder as an elasto-plastic continuum with time-dependent material properties and validated against experimentally observed plastic collapse. Suiker [14, 26] derived analytical expressions for elastic and plastic buckling of printed walls, providing closed-form estimates of the critical number of layers. Ooms et al. [17] developed a parametric CG framework with Mohr–Coulomb plasticity and automated element activation, extending buildability prediction to arbitrary print geometries. Kruger et al. [24, 30, 31] derived analytical lower-bound estimates of the critical layer count from thixotropic structuration models calibrated with rheometry. These models have demonstrated capability for horizontal deposition, where the failure mode is invariably buckling or plastic collapse and the interlayer interfaces remain intact. None of these frameworks, however, can represent interlayer delamination. The shared-node topology of the CG discretization enforces displacement continuity across every element boundary by construction, precluding the displacement jumps that characterize interface separation.

A parallel body of work has addressed the rheological characterization of printable concretes, establishing the material models on which part-level simulations depend. The linear structuration model of Roussel [32, 33], in which the static yield stress grows linearly with rest time, has become the standard constitutive description for the early-age evolution of cementitious materials in the 3DCP literature. Extensions to this model include the incorporation of plastic viscosity evolution [27, 34], critical elastic strain measurements via oscillatory rheometry [23, 33], and the characterization of interlayer bond strength as a function of rest time and surface moisture [35–37]. The last of these is the experimental quantity that governs an interface's resistance to delamination. These experimental advances provide the input parameters required by buildability simulations. The simulation frameworks themselves, however, have not yet evolved to exploit the full range of failure mechanisms that these parameters govern.

Emerging print strategies deposit layers at arbitrary orientations relative to the gravity vector (Figure 1) [4, 6, 9, 10, 38–41]. In these configurations, self-weight loads layer interfaces in shear and tension rather than pure compression, and interlayer delamination becomes a viable failure mechanism alongside the bulk mechanisms of plastic collapse and buckling. Delamination originates at any interface where two layers are in contact, and the strength of that bond is set by the rheological state of the substrate at the moment the second layer is deposited against it [23, 35]. When the substrate is still soft, the incoming material intermixes with it and the deposition pressure deforms the surface, producing mechanical interlocking and a strong, continuous bond. When the substrate has stiffened over a longer rest time, intermixing is suppressed, the contact pressure can no longer reshape the surface, and a weak cold joint forms [35, 42]; surface drying and moisture loss over the same interval further degrade the interface [36, 37]. The conditions that produce a weak bond therefore combine a long rest time before contact with anything that accelerates substrate stiffening or limits the mechanical interlock: long inter-layer intervals, as arise in large parts or long per-layer toolpaths; high accelerator dosages that raise the substrate yield stress rapidly even at short rest times; and low deposition pressures that reduce surface deformation and intermixing. Whether such a bond is actually challenged then depends on the layer orientation: non-horizontal deposition subjects the interface to the tension and shear that drive separation, whereas horizontal stacking holds it in compression. The governing failure mode thus depends on the interplay between geometry, print sequence, layer orientation, and structuration rate.

Accounting for delamination matters most for precisely the geometries that motivate 3DCP in the first place. Horizontal, compression-dominated walls rarely challenge the interface, but the overhanging, cantilevering, and non-planar forms that yield the largest gains in material efficiency and structural performance (Figure 1) load the interlayer bonds directly, making delamination a primary constraint on what can be built [4, 41]. The consequence is twofold. During printing, a bond that cannot carry the accumulating self-weight separates and the structure collapses before the geometry is complete. After hardening, a cold joint persists as a plane of weakness that lowers the load-bearing capacity and durability of the finished element [2, 36]. Capturing interlayer separation is therefore a prerequisite for extending buildability prediction beyond horizontal walls to the non-horizontal, structurally optimized geometries that the technology uniquely enables.

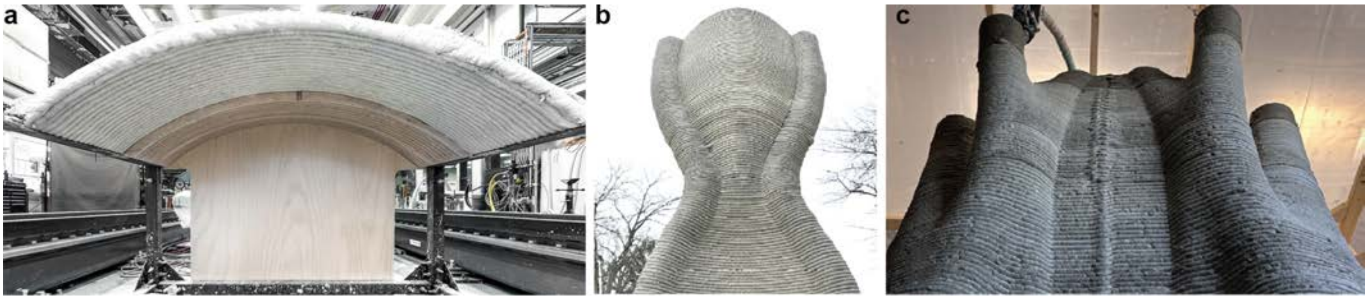

Figure 1: Representative 3DCP structures fabricated at the University of Michigan DART Laboratory with non-horizontal layer deposition, illustrating the buildability challenges addressed in this work. **(a)** Barrel vault with layers oriented along the curvature, creating interlayer interfaces loaded in combined shear and tension under self-weight [41]. **(b)** Printed RC wall prototype with non-planar layers demonstrating up to 60% material savings [9]. **(c)** Multi-branch structure during printing, where progressive self-weight accumulation on material with evolving fresh-state properties governs whether the structure fails by bulk plastic collapse or interlayer delamination [9].

Discontinuous Galerkin (DG) methods [43, 44] do not enforce displacement continuity, thus removing the limitation of CG methods: each element carries independent degrees of freedom, and whether a given face behaves as a bonded interface or a potential crack surface is set by the coupling terms applied to it in the variational form rather than by the mesh connectivity. DG formulations with cohesive interfaces have been applied to brittle fracture [45], composite delamination [46, 47], and dynamic crack propagation [48, 49]. More broadly, hybrid continuous/discontinuous frameworks that embed interface elements within a bulk discretization have been extended to reinforced concrete failure, including crack propagation, bond slip, and stress redistribution [50]. However, none of these formulations have been applied to 3DCP buildability, where progressive element activation, time-dependent elasto-viscoplastic bulk behavior, and structuration-dependent bond quality introduce requirements that existing frameworks do not address. Specifically, the DG cohesive frameworks of Noels and Radovitzky [44, 45], Mergheim et al. [51], and Wells and Sluys [52] assume time-independent bulk constitutive behavior and a fixed spatial domain, and do not include an activation mechanism for progressive material deposition.

This paper extends the DG cohesive approach to a setting where the domain grows during the simulation, the bulk and interface properties evolve with material age, and the bond quality at each interface is determined by the deposition history. Specifically, this paper develops a DG finite element method for part-level buildability simulation in 3DCP that captures plastic collapse and interlayer delamination within a unified formulation. Section 2 develops the formulation, proceeding from the governing equations and DG discretization through the element activation mechanism, the constitutive framework, and the assembled variational form. Section 3 presents the verification tests. Section 4 validates the framework against experimental observations of plastic collapse and interlayer delamination. Section 5 discusses the results, limitations, and directions for future work.

2. Methods

2.1. Problem definition and governing equations

In 3DCP, material is deposited sequentially along a prescribed toolpath, and each newly placed element must be sustained by material whose mechanical properties are evolving from those of a soft paste toward those of a load-bearing solid. The simulation must therefore represent a domain that grows with each deposition event, material properties that change continuously as functions of concrete age, and interfaces between layers whose integrity depends on the rheological conditions at the moment of contact.

The printed structure is represented by a fixed reference domain $\Omega \subset \mathbb{R}^3$ encompassing the complete geometry of all layers, including those not yet deposited. Elements are progressively activated as the print head advances, so that at any instant only a subset of the mesh carries mechanical load. The domain boundary $\partial\Omega$ is partitioned into a Dirichlet boundary Γ_{D}, where prescribed displacement conditions are imposed at the structural supports, and traction-free surfaces.

Within the DG discretization on mesh $\mathcal{T}_h$, every interior facet separates two adjacent elements whose displacement fields are independent by construction. These facets are classified according to their relationship to the print layer structure. Facets shared by elements deposited within the same layer are classified as intra-layer facets $\Gamma_{\mathrm{c}}^{\mathrm{intra}}$; no physical interface exists within a single deposited bead, and these faces should behave as if the material were continuous. Facets shared by elements belonging to different layers are classified as inter-layer facets $\Gamma_{\mathrm{c}}^{\mathrm{inter}}$; these correspond to physical interlayer boundaries where delamination may occur (Fig. 2).

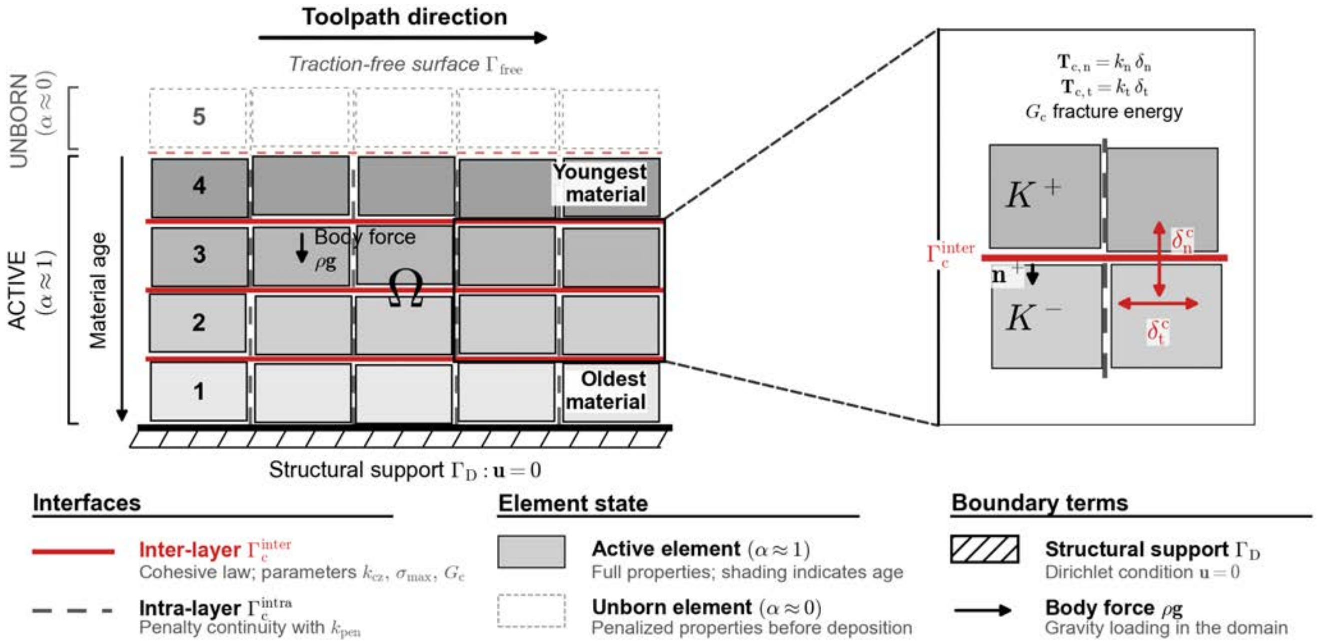

Figure 2: Problem domain and interface classification. Interior element facets are classified as intra-layer $\Gamma_{\mathrm{c}}^{\mathrm{intra}}$ (bonded via SIPG) or inter-layer $\Gamma_{\mathrm{c}}^{\mathrm{inter}}$ (governed by a cohesive law). Dirichlet conditions are applied at the structural supports Γ_{D}.

The presented formulation rests on the following modeling assumptions:

1. Quasi-static equilibrium. Inertial effects are neglected, as printing speeds are slow relative to mechanical wave propagation in the deposited material.

2. Infinitesimal (small) strains. The framework resolves the response up to the onset of buildability failure, the point at which the structure can no longer sustain the next deposition increment, rather than the post-failure collapse. Under this assumption the strain measure is linearized and equilibrium is written on the undeformed reference geometry, so the geometric stiffness is omitted. This is an approximation rather than an exact description: fresh and hardening concrete can develop appreciable strain in both the elastic and the viscoplastic regimes, and the overall deflection is not strictly infinitesimal. It is adopted because the objective is to identify when failure initiates, not to trace the large-deformation collapse that follows, and it remains acceptable for the deviatoric yielding and interlayer decohesion that govern at modest deflection. The assumption is not valid in two regimes: when deflections grow large enough to redistribute the load path, and when a geometric instability governs, since elastic or plastic buckling requires the geometric stiffness that arises only in a finite-deformation framework. A finite-deformation extension that removes this restriction is outlined in Section 5.

3. Homogeneous, isotropic, time-dependent elasto-viscoplastic bulk behavior. All mechanical properties are derived from measurable rheological quantities that evolve as functions of concrete age since deposition. The anisotropy introduced by the layered construction process is not modeled within the bulk material of the same layer; it is captured entirely through the cohesive interface law at interlayer boundaries between different layers (Section 2.4.3), i.e., any anisotropy introduced through intra-layer interfaces is neglected.

4. Yielding governed by a von Mises yield surface with Perzyna viscoplastic regularization. Fresh cementitious materials exhibit pressure-sensitive behavior [13, 53, 54]; however, the dominant in-process loading during printing is deviatoric—self-weight induces bending, shear, and torsion in unsupported regions—and the hydrostatic contribution remains comparatively small. The von Mises criterion is therefore adopted as a constitutive approximation appropriate for this loading regime. The framework accommodates pressure-dependent criteria such as Drucker–Prager [15, 29, 55] without modification to the DG formulation or the solution algorithm; only the yield function and flow direction require substitution. This extension is not pursued in this paper.

5. Mixed-mode (Mode I/II) cohesive failure [56–58] at inter-layer interfaces. The strength and fracture energy of each inter-layer bond depend on the rheological state of the substrate at the moment the subsequent layer is deposited; the specific model used to quantify this dependence is developed in Section 2.4.3.

6. The only applied load is gravitational self-weight. Other in-process loads such as nozzle contact pressure, thermal gradients, and environmental actions can be incorporated as additional surface traction or volumetric source terms but are not included in the present study.

Under these assumptions, the displacement field $\mathbf{u} : \Omega \to \mathbb{R}^3$ satisfies the balance of linear momentum [59–61],

$$-\nabla \cdot \boldsymbol{\sigma} = \mathbf{f} \quad \text{in } \Omega, \tag{1}$$

where $\boldsymbol{\sigma}$ denotes the Cauchy stress tensor and $\mathbf{f} = -\rho g\, \mathbf{e}_z$ is the gravitational body force, in which ρ is the mass density of the concrete, g is the magnitude of gravitational acceleration, and $\mathbf{e}_z$ is the unit basis vector corresponding to the vertical axis of the global coordinate system, directed opposite to the gravitational field. Homogeneous Dirichlet conditions are imposed at the structural supports, $\mathbf{u} = \mathbf{0}$ on Γ_D. The interlayer interface condition and its weak enforcement are developed in Sections 2.4.3 and 2.4.4.

The formulation is implemented in Python using the FEniCSx finite element framework [62], which provides the DOLFINx problem-solving environment, UFL (Unified Form Language) [63] for symbolic specification of variational forms, and Basix [64] for finite element basis function tabulation. The discrete systems are assembled into PETSc [65] sparse matrices and solved using its KSP linear solver interface with GMRES [66] preconditioned by the algebraic multigrid method GAMG or alternatively by the direct solver MUMPS [67] for smaller problems or debugging purposes. Mesh generation and hexahedral partitioning are performed with Gmsh [68]. The Jacobian is obtained by automatic differentiation of the UFL variational form.

2.2. *Discontinuous Galerkin formulation*

DG methods allow each element its own independent set of degrees of freedom, with no shared nodes between neighboring elements. The displacement field is therefore discontinuous across every interior facet by default. While the facets themselves are generated by the mesh, the mechanical role of a given facet, whether it acts as a bonded interface (no jump permitted) or as a potential failure surface (jump permitted), is set by the coupling terms applied to it in the variational form rather than by the mesh connectivity.

This makes DG naturally suited to the dual interface treatment required here: intra-layer facets are bonded, inter-layer facets may separate. This is the feature that sets the present formulation apart from continuum models of 3DCP buildability, in which contacting layers merge into a single continuous body: treating the interlayer boundary as a surface that can open admits delamination as a failure mode.

The domain Ω is discretized into a conforming hexahedral mesh $\mathcal{T}_h$. The displacement is approximated in a piecewise trilinear polynomial space with no inter-element continuity constraint:

$$V_h = \{\mathbf{v} \in [L^2(\Omega)]^3 \ : \ \mathbf{v}\big|_K \in [\mathbb{Q}^1(K)]^3, \ \forall\, K \in \mathcal{T}_h\}. \tag{2}$$

Because the displacement is discontinuous, quantities on a shared face F between elements K^+ and K^- are double-valued. Two operators are used throughout the formulation to work with these double-valued fields [43, 69]. The average operator $\{\boldsymbol{\phi}\} = \frac{1}{2}(\boldsymbol{\phi}^+ + \boldsymbol{\phi}^-)$ returns the mean of the two sides, and the jump operator $[\![\boldsymbol{\phi}]\!] = \boldsymbol{\phi}^+ - \boldsymbol{\phi}^-$ returns the difference, where $\mathbf{n}$ is the unit normal directed from K^+ to K^-.

The two face types identified in Section 2.1 receive different coupling terms. On intra-layer faces $\Gamma_\mathrm{c}^\mathrm{intra}$, where no physical interface exists and the material should behave as a bonded continuum, the Symmetric Interior Penalty Galerkin (SIPG) method [69] is used to weakly enforce displacement continuity. The SIPG method penalizes the displacement jump across the face while maintaining consistency and symmetry of the bilinear form, so that the DG solution converges to the continuous solution as the mesh is refined. On inter-layer faces $\Gamma_\mathrm{c}^\mathrm{inter}$, where delamination may occur, the SIPG terms are omitted entirely. Instead, the sole coupling between the two elements is provided by the cohesive traction $\mathbf{T}_\mathrm{c}$ (Eqs. (18)–(20)), which degrades with damage and can vanish completely when the interface fails. Applying SIPG terms on inter-layer faces would enforce an additional continuity constraint that prevents the interface from opening, defeating the purpose of the cohesive law (Fig. 3).

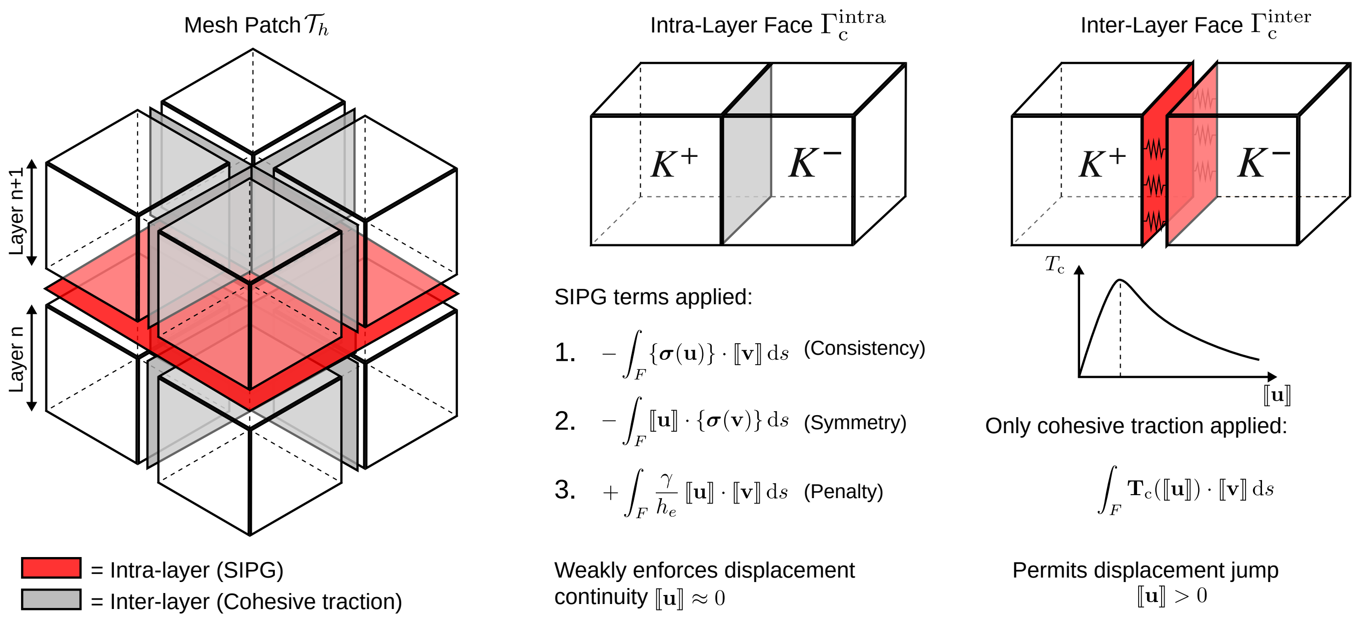

Figure 3: Dual interface treatment. On intra-layer faces $\Gamma_\mathrm{c}^\mathrm{intra}$, the SIPG method enforces displacement continuity. On inter-layer faces $\Gamma_\mathrm{c}^\mathrm{inter}$, only the cohesive traction $\mathbf{T}_\mathrm{c}$ is applied.

2.3. Element activation

The mesh $\mathcal{T}_h$ represents the complete printed geometry, including layers that have not yet been deposited at the current simulation time. Elements that have not yet been deposited must be prevented from contributing stiffness or load to the system, and must begin contributing at the appropriate time as the print head advances.

Each element e is assigned a birth time t_b^e computed from the cumulative distance of its centroid along the toolpath and the tool center point speed: $t_\mathrm{b}^e = d_e/v_\mathrm{TCP}$, where d_e is the cumulative distance from the toolpath origin to the centroid of element e and v_TCP is the tool center point velocity. An element is considered unborn when $t < t_\mathrm{b}^e$ and fully deposited when $t \gg t_\mathrm{b}^e$. Rather than switching the element on instantaneously at $t = t_\mathrm{b}^e$, which would introduce a discontinuity in the global stiffness matrix and degrade Newton convergence, the transition is smoothed by a scalar activation function [70, 71]:

$$\alpha^e(t) = \alpha_\mathrm{min} + (1 - \alpha_\mathrm{min}) \cdot \tfrac{1}{2}\left(1 + \tanh(\kappa\,(t - t_\mathrm{b}^e))\right). \tag{3}$$

The function transitions from α_min (unborn) to 1 (fully active) over a narrow interval centered at t_b^e. The parameter $\alpha_\mathrm{min} \ll 1$ is a small floor that prevents the element stiffness matrix from becoming singular before deposition, and κ (s^{-1}) controls how rapidly the transition occurs. All contributions of element e to the variational form—bulk stress, body force, and interface terms—are multiplied by α^e, so that an unborn element has negligible effect on the global system while remaining algebraically present in the mesh.

The mesh holds the complete geometry from the outset, including layers not yet deposited, so the assembled system carries the full degree-of-freedom count even when only a few elements are active. This nominal size, however, does not translate into a proportional computational cost, for two reasons. First, the degrees of freedom of unborn elements are pinned to zero (Section 2.5) by replacing their Jacobian rows and columns with identity entries and zeroing the corresponding residual, which turns them into independent trivial equations of the form $u_i = 0$ that are decoupled from the active block. The linear solver therefore expends negligible effort on them, and the effective cost tracks the number of active degrees of freedom rather than the nominal total. Second, keeping the full mesh in place means the sparsity pattern and degree-of-freedom numbering are established once and reused at every step, and the viscoplastic and damage history variables stay attached to fixed quadrature points and facets throughout the simulation.

Restricting the assembly to the active elements would reduce the nominal system size, but it would require rebuilding the index map and the matrix sparsity pattern each time an element is deposited, and re-interpolating the history variables onto the changing active set. The fixed-mesh strategy trades the modest memory overhead of carrying the inactive degrees of freedom for the avoidance of this per-step bookkeeping and for a constant matrix structure that is efficient to reuse.

The activation of interface terms on shared faces requires separate treatment for the two face types. On intra-layer faces, the SIPG terms enforce displacement continuity between elements within the same layer. This coupling should only engage when both adjacent elements have been deposited; the facet activation is therefore taken as the minimum of the two element activations, $\alpha_\mathrm{f} = \min(\alpha^+, \alpha^-)$, which remains near zero until both sides are active.

On inter-layer cohesive faces, the opposite convention is adopted: $\alpha_\mathrm{f}^\mathrm{coh} = \max(\alpha^+, \alpha^-)$. This does not cause the interface to transmit traction before both layers exist. Degrees of freedom belonging to unborn elements are pinned to zero displacement (Section 2.5), so the displacement jump $[\![\mathbf{u}]\!]$ across a cohesive face where one side is unborn is identically zero, and the cohesive traction $\mathbf{T}_\mathrm{c}$ vanishes accordingly. The purpose of the max convention is to ensure that the cohesive stiffness is already present at the substrate's activation level at the instant the new layer arrives, providing a smooth onset of interlayer coupling without requiring a separate contact-detection algorithm.

2.4. Constitutive modeling

Freshly printed concrete is neither a classical solid nor a classical fluid. At the moment of extrusion it behaves as a viscoplastic paste [23, 72], flowing under sufficient stress but retaining its shape otherwise. Over the following minutes to hours, chemical hydration and physical structuration progressively stiffen the material, expand its elastic domain, and transform it into a load-bearing solid. A constitutive model for 3DCP must capture this continuous transition using quantities accessible through standard laboratory characterization.

The approach adopted here is to derive all mechanical properties from a small set of rheological inputs (Table 1). The yield stress τ_0, the most commonly measured rheological property in the 3DCP literature [23, 27, 73], serves as a proxy for the overall state of structuration, and all other stiffness and strength parameters are related to it. This ensures internal consistency: as the material ages and τ_0 increases, the elastic modulus, yield surface, and interfacial strength evolve in a physically coupled manner. Because these parameters are intrinsic to the specific cementitious formulation and printing conditions employed, no universally applicable values exist; Table 1 therefore lists each input parameter alongside the standard experimental protocol through which it can be determined for a given material system. The specific values adopted for validation are reported in Section 4.2.

2.4.1. Structuration and time-dependent property evolution

The yield stress is the primary quantity governing the evolving mechanical state of the deposited material. Following the thixotropic structuration model of Roussel [32], the static yield stress grows linearly with the elapsed time since deposition:

$$\tau_0(t_{age}) = \tau_{0,0} + A_\mathrm{thix} \cdot t_{age}, \tag{4}$$

Table 1: Rheological and mechanical input parameters.

Parameter	Symbol	Unit	Measurement
Initial static yield stress	$\tau_{0,0}$	Pa	Vane shear test [74, 75]
Structuration rate	A_{thix}	Pa/s	Time-dependent vane test [32]
Plastic viscosity	μ_p	Pa s	Rotational rheometry [76]
Critical elastic strain	γ_c	–	Oscillatory rheometry (LVER) [33]
Poisson's ratio (fresh)	ν_{fresh}	–	Ultrasonic [77] or assumed
Poisson's ratio (hardened)	ν_{hard}	–	Ultrasonic [77] or assumed
Hardened Young's modulus	E_∞	MPa	Compression test
Setting time	t_{set}	s	Vicat or penetration test [78]
Density	ρ	kg/m^3	Gravimetric
Mode I fracture energy	G_{Ic}	N/mm	Wedge splitting test [79]
Mode II fracture energy	G_{IIc}	N/mm	Shear bond test [2]

where $t_{age} = t - t_\text{b}$ is the material age (elapsed time since the element's birth time t_b), $\tau_{0,0}$ is the initial static yield stress upon extrusion, and A_{thix} is the structuration rate. The vane shear test (Table 1) characterizes the static yield stress while the material behaves as a yield-stress fluid, which is the regime present at deposition and through the early-age window in which buildability is decided. It is used here to identify the initial yield stress $\tau_{0,0}$ and the structuration rate A_{thix}; the yield stress at later ages then follows from the structuration law (Eq. (4)) rather than from a vane measurement on the stiffened material. As the substrate hardens and its response becomes solid-like, the vane test loses validity, and a hardened-state yield stress is better obtained from penetration [74] or unconfined compression tests. The constitutive model depends only on the value of τ_0, not on the method used to obtain it, so it accepts the yield stress from whichever protocol is appropriate to the age range of interest.

The elastic stiffness is derived from the yield stress without requiring an independent modulus measurement. Oscillatory rheometry studies [33] establish that cementitious pastes respond linearly up to a critical strain γ_c, beyond which the microstructure yields. Within this linear viscoelastic region (LVER), the shear modulus is the ratio of the stress at yield to the strain at yield, giving $G \approx \tau_0/\gamma_c$ [23]. Because τ_0 grows with age, G increases proportionally, capturing the progressive stiffening of the paste. To prevent this rheology-derived estimate from exceeding the physical elastic stiffness of hardened concrete, the shear modulus is capped at the value corresponding to the fully hardened Young's modulus E_∞:

$$G(t_{age}) = \min\left(\frac{\tau_0(t_{age})}{\gamma_c},\ \frac{E_\infty}{2(1+\nu_{\text{hard}})}\right). \tag{5}$$

The Young's modulus follows from Hooke's law [59, 80] for isotropic elasticity, $E(t_{age}) = 2\,G(t_{age})\,(1+\nu(t_{age}))$. The Poisson's ratio is modeled as an exponential transition from a near-incompressible fresh state ($\nu_{\text{fresh}} \approx 0.48$) to a hardened value ($\nu_{\text{hard}} \approx 0.20$) [71, 77], reflecting the change from nearly isochoric deformation in the fresh paste to significant volumetric stiffness in the hardened solid:

$$\nu(t_{age}) = \nu_{\text{hard}} + (\nu_{\text{fresh}} - \nu_{\text{hard}})\ \exp(-t_{age}/t_{\text{set}}). \tag{6}$$

The plastic viscosity grows exponentially with the same characteristic time [27, 71], reflecting the increasing resistance to plastic flow as the internal structure builds, given by:

$$\eta(t_{age}) = \mu_p\ \exp(t_{age}/t_{\text{set}}). \tag{7}$$

The Lamé parameters [59, 80] λ and $\mu = G$ are computed from E and ν through the standard isotropic relations (Fig. 4).

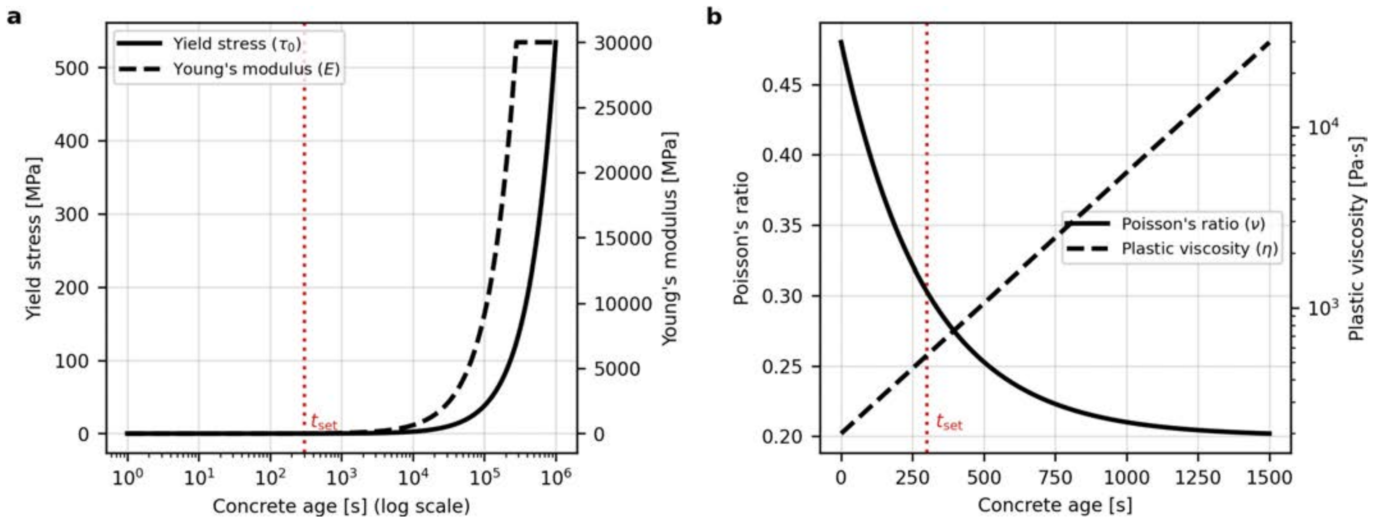

Figure 4: Time-dependent material property evolution as a function of concrete age t_{age}. (a) Yield stress and Young's modulus increase with structuration; the modulus is capped at the hardened value E_∞. (b) Poisson's ratio decays from a near-incompressible fresh state to a hardened value, while plastic viscosity grows exponentially.

2.4.2. Elasto-viscoplastic bulk model

When the stress in a freshly printed element remains below the yield stress, the material responds elastically. When the stress exceeds the yield stress—as occurs when unsupported regions generate bending moments that surpass the material's evolving capacity—the material flows viscoplastically and permanent strain accumulates. As structuration proceeds, the yield stress grows and the viscosity increases, making the material progressively more resistant to deformation. This transition from a deformable paste to a rigid solid is the mechanism that governs buildability.

Under the small-strain assumption, the total strain is additively decomposed into elastic and viscoplastic contributions [81], $\boldsymbol{\varepsilon} = \boldsymbol{\varepsilon}^e + \boldsymbol{\varepsilon}^{vp}$, where $\boldsymbol{\varepsilon}(\mathbf{u}) = \frac{1}{2}(\nabla\mathbf{u} + \nabla\mathbf{u}^T)$ is the strain rate tensor [59, 80]. The elastic strain $\boldsymbol{\varepsilon}^e$ is the recoverable portion that produces stress through the constitutive law, while the viscoplastic strain $\boldsymbol{\varepsilon}^{vp}$ represents the permanent deformation that has accumulated through plastic flow. The elastic strain is obtained by subtraction, $\boldsymbol{\varepsilon}^e = \boldsymbol{\varepsilon} - \boldsymbol{\varepsilon}^{vp}$, and the evolution of $\boldsymbol{\varepsilon}^{vp}$ is governed by the Perzyna flow rule (Eq. (10)). A similar partitioned strategy, advancing the constitutive law explicitly through sub-stepping, has been used in fluid-solid elasto-viscoplastic models of 3DCP [15]. The Cauchy stress is determined by the elastic strain alone [59, 80], according to:

$$\boldsymbol{\sigma} = \lambda(t_{age})\,\mathrm{tr}(\boldsymbol{\varepsilon}^e)\,\mathbf{I} + 2\,\mu(t_{age})\,\boldsymbol{\varepsilon}^e. \tag{8}$$

Yielding is governed by the von Mises yield function [82], given by:

$$f(\boldsymbol{\sigma},\, t_{age}) = \sigma_{\mathrm{vm}} - \sigma_{\mathrm{y}}(t_{age}) \le 0, \tag{9}$$

where $\sigma_{\mathrm{vm}} = \sqrt{3J_2}$ is the von Mises equivalent stress, $J_2 = \frac{1}{2}\,\mathbf{s} : \mathbf{s}$ is the second invariant of the deviatoric stress $\mathbf{s}$ [59, 80], and $\sigma_{\mathrm{y}}(t_{age}) = \sqrt{3}\;\tau_0(t_{age})$ is the uniaxial yield stress. As the material ages and τ_0 increases, σ_{y} increases proportionally, expanding the elastic domain and suppressing viscoplastic flow.

The rate of viscoplastic strain accumulation is governed by a Perzyna-type overstress model [81]. The Perzyna formulation is well suited to cementitious materials because it provides a smooth, rate-dependent transition between elastic and plastic behavior—consistent with the rheological response of Bingham-like pastes [83], in which the material flows at a rate proportional to the excess stress above the yield point, via:

$$\dot{\boldsymbol{\varepsilon}}^{vp} = \frac{1}{2\,\eta(t_{age})}\left\langle f(\boldsymbol{\sigma},\, t_{age})\right\rangle \frac{\mathbf{s}}{\|\mathbf{s}\|}, \tag{10}$$

where $\eta(t_{age})$ is the age-dependent plastic viscosity (Eq. (7)), $\langle\cdot\rangle$ denotes the Macaulay bracket ($\langle x\rangle = x$ if $x > 0$, else 0), and $\mathbf{s}/\|\mathbf{s}\|$ is the deviatoric flow direction. The viscosity governs the rate of plastic flow for a given overstress and defines a natural relaxation time scale η/E over which the material returns toward the yield surface. As η increases with age, the same overstress produces progressively less viscoplastic flow.

The simulation advances in discrete time increments Δt, each representing a stage of the printing process during which new material may be deposited and existing material continues to age. Within each increment, two coupled quantities must be determined: the displacement field $\mathbf{u}$ and the viscoplastic strain $\boldsymbol{\varepsilon}^{vp}$. These are interdependent: the displacement determines the stress, and the stress determines how much plastic flow occurs. Solving for both simultaneously would require a Jacobian that accounts for their mutual dependence. The present work instead adopts a partitioned approach [84] in which the two are resolved sequentially. First, the equilibrium problem is solved with $\boldsymbol{\varepsilon}^{vp}$ frozen at its value from the previous converged step; because the viscoplastic strain does not change during the Newton iterations, the stress (Eq. (8)) depends linearly on the displacement, and the Jacobian reduces to the elastic stiffness matrix. Second, once equilibrium has converged, the viscoplastic strain is updated from the converged stress state using the Perzyna flow rule (Eq. (10)).

This viscoplastic update evaluates the flow rule at the converged stress and applies the resulting strain increment over Δt. If the time increment is small, this produces a modest strain correction and the result is accurate. If Δt is large, however, the accumulated plastic strain can be large enough to invalidate the stress state from which it was computed, producing an inaccurate or unstable result. Stability analysis of the explicit integration applied to the linearized Perzyna flow rule shows that the maximum permissible substep is governed by the ratio of the plastic viscosity to the elastic modulus, $\Delta t_{\text{sub}} \leq \eta/E$ [15, 85]. Physically, η/E is the time scale over which the material can redistribute stress through viscoplastic flow: a stiffer material (large E) or a less viscous one (small η) responds faster and therefore requires a smaller substep. When Δt exceeds η/E, the update is subdivided into $n_{\text{sub}} = \lceil \Delta t/(\eta/E) \rceil$ substeps. Because only cells that are actively yielding ($f > 0$) require this integration, the additional cost is confined to the yielding portion of the mesh.

The explicit update of the viscoplastic strain is only conditionally stable: if the substep is too large relative to the rate at which the material relaxes stress through viscous flow, the integration error grows rather than decays. The stability limit, $\Delta t_{\text{sub}} \leq \eta/E$, is set by the ratio η/E, which has units of time and is the relaxation time of the material, the characteristic time over which an overstress is dissipated by viscoplastic flow. Because η and E both evolve with concrete age (Eqs. (7) and (5)), this relaxation time is not a single fixed value; it is computed for each yielding cell from that cell's current η and E at the current step. Fresh material has a low viscosity and therefore a short relaxation time, so it requires fine substepping; as the material stiffens and its viscosity grows, the relaxation time lengthens and a larger substep becomes admissible.

The limit is independent of how far the stress lies above the yield surface. The overstress $\langle f \rangle$ controls how much viscoplastic strain accumulates in a given step, but not the largest stable step, so a cell just past yield and a cell deep in the flow regime share the same limit, since the stability analysis depends on the relaxation time η/E alone. In the unyielded, elastic regime $f \leq 0$ and the Macaulay bracket sets $\dot{\boldsymbol{\varepsilon}}^{vp} = \mathbf{0}$, so there is no viscoplastic strain to integrate and the limit is not invoked; the substepping is applied only to cells with $f > 0$ (Algorithm 1). The condition therefore changes with the material state only through the age-dependent η and E, evaluated cell by cell, and not through the stress level.

Because the equilibrium problem is solved with the viscoplastic strain and damage history frozen at their previous values and both quantities are updated explicitly afterward, the overall time-stepping procedure is conditionally stable. Accuracy therefore requires that the time increment Δt be sufficiently small for the explicit constitutive updates to remain valid. The time increment is a user-specified parameter that controls the number of simulation steps used to resolve the complete deposition sequence. When Δt exceeds the local viscoplastic stability bound η/E, the adaptive substepping procedure described above automatically subdivides the constitutive update into substeps of size $\Delta t_{\text{sub}} \leq \eta/E$, ensuring bounded integration error regardless of the chosen macro step. The values of Δt used in the validation cases are reported in Section 4.

2.4.3. Mixed-mode cohesive interface law with structuration-dependent bond quality

The bulk model governs the response within each deposited filament, but it does not by itself determine whether two successive layers remain bonded. In 3D concrete printing, neighboring layers may separate or slide relative to one another under gravity-driven bending and shear. The DG formulation described in Section 2.2 admits displacement jumps across inter-layer faces, so the bond between layers must be supplied explicitly through an interface law.

In the present model, that coupling is provided entirely by a cohesive traction $\mathbf{T}_{\text{c}}$ acting on each inter-layer face. This traction is the only mechanism transmitting forces between adjacent layers: if it degrades to zero, the interface loses its load-carrying capacity and the layers separate. The cohesive law must therefore describe how the interface resists both tensile opening and tangential sliding, and how that resistance progressively degrades as damage accumulates. Moreover, the quality of the bond between two layers depends on the rheological state of the substrate at the moment the new layer is deposited [23]: a short rest time yields a strong bond through mechanical intermixing, whereas a long rest time produces a weak bond—a cold joint [35]. The development below proceeds from the kinematic decomposition of the displacement jump, through the bond quality and the interface parameters it governs, to the damage evolution and the resulting traction–separation response.

Let $[\![\mathbf{u}]\!]$ denote the displacement jump across an inter-layer face. With $\mathbf{n}^+$ the outward unit normal of element K^+, the jump is decomposed into normal and tangential parts as

$$\delta_{\text{n}} = [\![\mathbf{u}]\!] \cdot \mathbf{n}^+, \qquad \boldsymbol{\delta}_{\text{t}} = [\![\mathbf{u}]\!] - \delta_{\text{n}}\, \mathbf{n}^+, \tag{11}$$

where δ_{n} measures opening or compression normal to the interface, and $\boldsymbol{\delta}_{\text{t}}$ measures sliding in the interface plane.

The rest time at an inter-layer face is determined by the birth times of the two adjacent elements, $\Delta t_{\text{rest}} = |t_{\text{b}}^B - t_{\text{b}}^A|$. During this interval the substrate structures according to Eq. (4), reaching a yield stress of $\tau_{\text{sub}} = \tau_{0,0} + A_{\text{thix}} \cdot \Delta t_{\text{rest}}$. The bond quality is quantified by a dimensionless parameter $\beta_{\text{bond}} \in (0, 1]$ based on the ratio of nozzle deposition pressure p_{dep} to substrate yield stress:

$$\beta_{\text{bond}} = 1 - \exp\left(-\frac{p_{\text{dep}}}{\tau_{\text{sub}}}\right). \tag{12}$$

The quantity p_{dep} is an effective deposition pressure: the mean pressure that forces the incoming filament into the substrate under the finite gap between the nozzle and the previous layer. It is determined as the steady-state line pressure during deposition minus the steady-state pressure during free extrusion at the same volumetric flow rate,

$$p_{\text{dep}} = \overline{P}_{\text{print}} - \overline{P}_{\text{open}}, \tag{13}$$

the contact-pressure definition introduced for material-extrusion additive manufacturing by Coogan and Kazmer [86] and developed further by Kim et al. [87]. Because both pressures are measured at the same flow rate, their difference cancels the flow resistance common to the two cases and isolates the pressure associated with confined deposition against the previous layer. It is a measurable process variable in cementitious printing, where the deposition pressure between the nozzle and the substrate tracks the extrusion pressure and increases with print velocity [88]. The quantity is obtained before the structural simulation and is therefore independent of the predicted failure; for the present study it is measured directly on the printing system, with the value reported in Section 4.

The ratio $\phi = p_{\mathrm{dep}}/\tau_{\mathrm{sub}}$ serves as a penetration index measuring the capacity of the nozzle pressure to deform the substrate surface and achieve mechanical interlocking. When τ_{sub} is small relative to p_{dep} (young substrate, short rest time), $\beta_{\mathrm{bond}} \to 1$. When τ_{sub} is large (aged substrate, long rest time, or high accelerator dosage), $\beta_{\mathrm{bond}} \to 0$ (Fig. 5a). The bond quality parameter is computed once per inter-layer facet at the simulation time when both adjacent elements have been activated, and remains constant thereafter.

The intrinsic cohesive response of a fully bonded interface is governed by a normal strength σ_{n}^0, a tangential strength τ_{s}^0, and mode I and mode II fracture energies G_{Ic} and G_{IIc}. These intrinsic strengths are identified with the bulk yield stresses of the adjacent material: $\sigma_{\mathrm{n}}^0 = \sigma_{\mathrm{y}}(t_{age})$ (the uniaxial yield stress, Eq. (9)) and $\tau_{\mathrm{s}}^0 = \tau_0(t_{age})$ (the shear yield stress, Eq. (4)). In 3D concrete printing, two modifications are necessary. First, the bulk yield stresses evolve with age through structuration (Eq. (4)), so the strengths that the interface can mobilize grow over time. Second, a poor initial bond permanently limits the fraction of that growing strength that the interface can actually transmit. Both effects are captured by scaling the intrinsic properties with β_{bond}.

The effective cohesive strengths combine the frozen bond quality with the evolving bulk response:

$$\sigma_{\mathrm{c}}(t) = \beta_{\mathrm{bond}}\, \bar{\sigma}_{\mathrm{n}}^0(t), \qquad \tau_{\mathrm{c}}(t) = \beta_{\mathrm{bond}}\, \bar{\tau}_{\mathrm{s}}^0(t), \tag{14}$$

where $\bar{\sigma}_{\mathrm{n}}^0(t)$ and $\bar{\tau}_{\mathrm{s}}^0(t)$ are the average intrinsic strengths of the two adjacent elements at the current simulation time. The strengths are time-dependent because the bulk material continues to stiffen after deposition: a young interface is weak because the concrete itself is weak, even if the bond quality is high.

The effective fracture energies, by contrast, are time-independent:

$$G_{\mathrm{Ic}}^{\mathrm{eff}} = \beta_{\mathrm{bond}}\, G_{\mathrm{Ic}}, \qquad G_{\mathrm{IIc}}^{\mathrm{eff}} = \beta_{\mathrm{bond}}\, G_{\mathrm{IIc}}. \tag{15}$$

This distinction reflects the underlying physics: the fracture energy is governed by the degree of mechanical interlocking established at the moment of contact, which is fixed once the interface forms. The cohesive strength, on the other hand, is limited by the weaker of the two adjacent layers, whose yield stress continues to grow with structuration.

A newly formed interface is therefore weak on two counts—both the bond quality and the bulk strength are low. As the layers age, the interface strengthens through the growth of $\bar{\sigma}_{\mathrm{n}}^0(t)$, but the permanent penalty of a poor initial bond persists through the frozen β_{bond}.

The interface stiffnesses K_{n} and K_{t} are chosen so that the total energy dissipated during complete separation equals the prescribed fracture toughness in each mode [56]:

$$K_{\mathrm{n}}(t) = \frac{\sigma_{\mathrm{c}}(t)^2}{2\,G_{\mathrm{Ic}}^{\mathrm{eff}}} = \frac{\beta_{\mathrm{bond}}\, \bar{\sigma}_{\mathrm{n}}^0(t)^2}{2\,G_{\mathrm{Ic}}}, \qquad K_{\mathrm{t}}(t) = \frac{\tau_{\mathrm{c}}(t)^2}{2\,G_{\mathrm{IIc}}^{\mathrm{eff}}} = \frac{\beta_{\mathrm{bond}}\, \bar{\tau}_{\mathrm{s}}^0(t)^2}{2\,G_{\mathrm{IIc}}}. \tag{16}$$

As the displacement jump grows, the interface progressively loses load-carrying capacity through a scalar damage variable $D \in [0,1]$, where $D = 0$ is an intact bond and $D = 1$ is complete decohesion. Damage is driven by the ratio of the displacement energy stored in each mode to the corresponding fracture energy, combined in an exponential law [89, 90]:

$$D = 1 - \exp\!\left(-\frac{\langle \delta_{\mathrm{n}} \rangle^2}{2\,G_{\mathrm{Ic}}^{\mathrm{eff}}/K_{\mathrm{n}}} - \frac{\|\boldsymbol{\delta}_{\mathrm{t}}\|^2}{2\,G_{\mathrm{IIc}}^{\mathrm{eff}}/K_{\mathrm{t}}} \right), \tag{17}$$

where the Macaulay bracket $\langle \delta_{\mathrm{n}} \rangle = \max(\delta_{\mathrm{n}}, 0)$ restricts the mode I contribution to tensile opening. As the normal opening or tangential sliding increases, D increases monotonically toward unity and the traction capacity diminishes. Damage is irreversible: a history variable $D_{\max}$ records the maximum value attained over the loading history, and the effective damage is taken as $D \leftarrow \max(D, D_{\max})$ (Fig. 5c).

Because K_{n} and K_{t} grow with structuration (Eq. (16)), the characteristic separations $\delta_{\mathrm{n}}^c = \sigma_{\mathrm{c}}/K_{\mathrm{n}} = 2\,G_{\mathrm{Ic}}^{\mathrm{eff}}/\sigma_{\mathrm{c}}$ and $\delta_{\mathrm{t}}^c = \tau_{\mathrm{c}}/K_{\mathrm{t}} = 2\,G_{\mathrm{IIc}}^{\mathrm{eff}}/\tau_{\mathrm{c}}$ decrease as the interface ages: a stiffer, stronger interface fails at a smaller displacement jump but dissipates the same total fracture energy G^{eff}. This is the standard scaling of cohesive zone models with fixed fracture energy and evolving strength, and is physically consistent with the transition from a ductile fresh paste to a brittle hardened solid.

The cohesive traction $\mathbf{T}_{\mathrm{c}}$ is decomposed into a normal component T_{n} perpendicular to the interface and a tangential component $\mathbf{T}_{\mathrm{t}}$ in the interface plane. The normal component must distinguish between two regimes. When the interface opens ($\delta_{\mathrm{n}} > 0$), the traction resists separation with a stiffness that degrades with damage. When the interface is in compression ($\delta_{\mathrm{n}} < 0$), damage is not relevant—compression does not weaken the interface. However, because the DG discretization assigns independent degrees of freedom to each element, there is no geometric constraint preventing two adjacent elements from numerically overlapping;

shared nodes in a CG method make such overlap impossible by construction, but in the DG formulation this non-overlapping condition must be enforced explicitly. The second term in the normal traction serves this purpose, applying a stiff undamaged penalty whenever $\delta_n < 0$:

$$T_n = \underbrace{[(1-D)\,K_n + D\,K_n^{res}]\,\langle\delta_n\rangle}_{\text{tension: damage-degraded}} + \underbrace{K_n\,\min(\delta_n,\,0)}_{\text{compression: contact penalty}}, \tag{18}$$

where $K_n^{res} = r\,K_n$ is a small residual stiffness retained at full damage to prevent a singular Jacobian. The tangential traction resists sliding in the interface plane and degrades symmetrically with damage:

$$\mathbf{T}_t = [(1-D)\,K_t + D\,K_t^{res}]\,\boldsymbol{\delta}_t. \tag{19}$$

The complete cohesive traction vector is:

$$\mathbf{T}_c = T_n\,\mathbf{n}^+ + \mathbf{T}_t. \tag{20}$$

The resulting traction–separation response is shown in Fig. 5b for several values of β_{bond}.

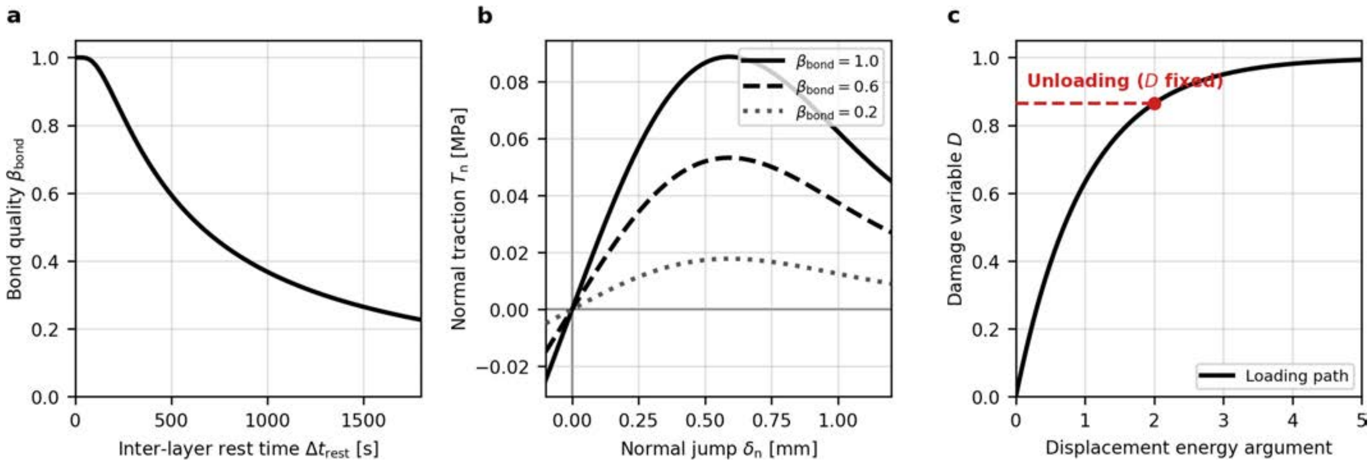

Figure 5: Mixed-mode cohesive interface law with structuration-dependent bond quality. (a) β_{bond} as a function of interlayer rest time. (b) Normal traction–separation response for several bond qualities. (c) Exponential damage evolution with irreversibility enforced by D_{max}.

2.4.4. Variational form

The preceding sections define the bulk constitutive response, the cohesive interface law, and the element activation function. The variational form assembles these contributions into a single nonlinear residual that is solved at each time step. The global problem is: find $\mathbf{u} \in V_h$ such that for all $\mathbf{v} \in V_h$:

$$F(\mathbf{u},\mathbf{v}) = F_{bulk} + F_{coh} + F_{SIP} + F_{stab} + F_{BC} + F_{grav} = 0. \tag{21}$$

Each term corresponds to a distinct physical or numerical contribution. The bulk term represents the internal stress resistance of the material within each element, weighted by the activation function α so that unborn elements do not contribute:

$$F_{bulk} = \int_\Omega \alpha\,\boldsymbol{\sigma} : \boldsymbol{\varepsilon}(\mathbf{v})\,d\Omega, \tag{22}$$

where the stress $\boldsymbol{\sigma} = \boldsymbol{\sigma}(\mathbf{u}, \boldsymbol{\varepsilon}^{vp}, t_{age})$ is computed from Eq. (8). The cohesive term transmits forces between adjacent layers through the traction law developed in Section 2.4.3, activated by the cohesive facet function α_f^{coh}:

$$F_{coh} = \int_{\Gamma_c^{inter}} \alpha_f^{coh}\,\mathbf{T}_c \cdot [\![\mathbf{v}]\!]\,dS, \tag{23}$$

On intra-layer faces, the SIPG method [69] weakly enforces displacement continuity through a consistency term that imposes the correct flux, a symmetry term that renders the bilinear form symmetric, and a penalty term that penalizes the displacement jump. Together these ensure that elements within the same layer behave as a bonded continuum:

$$F_{SIP} = \int_{\Gamma_c^{intra}} \alpha_f\,(-\{\boldsymbol{\sigma}(\mathbf{u})\}\,\mathbf{n}\cdot[\![\mathbf{v}]\!] - \{\boldsymbol{\sigma}(\mathbf{v})\}\,\mathbf{n}\cdot[\![\mathbf{u}]\!] + \gamma\,[\![\mathbf{u}]\!]\cdot[\![\mathbf{v}]\!])\,dS, \tag{24}$$

where $\gamma = c_\gamma\,\bar{E}/h$ is the SIP penalty parameter, $\bar{E}$ is the average Young's modulus of the two adjacent elements, and h is the element face diameter. A supplementary jump stabilization term on intra-layer faces provides additional resistance against spurious displacement discontinuities:

$$F_{stab} = \int_{\Gamma_c^{intra}} \alpha_f\,\gamma_{safe}\,[\![\mathbf{u}]\!]\cdot[\![\mathbf{v}]\!]\,dS, \tag{25}$$

where $\gamma_{\text{safe}} = c_{\text{safe}}\,\bar{E}/h$ with $c_{\text{safe}} \ll c_\gamma$. Dirichlet conditions at the structural supports are imposed weakly via Nitsche's method [91], which applies the same consistency–symmetry–penalty formulation used by the SIPG terms but at the external boundary rather than at interior faces:

$$F_{\text{BC}} = \int_{\Gamma_{\text{D}}} \alpha\,(-\boldsymbol{\sigma}(\mathbf{u})\,\mathbf{n}\cdot\mathbf{v} - \boldsymbol{\sigma}(\mathbf{v})\,\mathbf{n}\cdot\mathbf{u} + \gamma_{\text{D}}\,\mathbf{u}\cdot\mathbf{v})\,dS, \tag{26}$$

where $\gamma_{\text{D}} = c_{\text{D}}\,E/h$ is the Nitsche penalty. The gravitational body force represents the self-weight loading that drives deformation in the structure:

$$F_{\text{grav}} = \int_{\Omega} \alpha\,\rho\,g\,\mathbf{e}_z\cdot\mathbf{v}\,d\Omega. \tag{27}$$

The numerical parameters of the formulation are collected in Table 2. The penalty multipliers c_γ, c_{safe}, and c_{D} follow established scaling for DG discretizations of elasticity and were verified by mesh-sensitivity studies to provide stable convergence without materially affecting the computed structural response.

Table 2: Numerical parameters of the formulation.

Parameter	Symbol	Unit	Value
Interface and penalty parameters			
SIP penalty multiplier	c_γ	–	100
Jump stabilization multiplier	c_{safe}	–	0.05
Nitsche penalty multiplier	c_{D}	–	300
Residual stiffness ratio	r	–	0.05
Activation parameters			
Activation sharpness	κ	s^{-1}	1.0
Activation floor	α_{min}	–	10^{-10}
Solver settings			
Newton relative tolerance	tol_{rel}	–	10^{-5}
Newton absolute tolerance	tol_{abs}	–	10^{-10}
Minimum line-search step	ω_{min}	–	0.02
Armijo parameter	c_1	–	10^{-4}

2.5. Solution procedure

The variational form (Eq. (21)) is nonlinear due to the damage-dependent cohesive tractions and the activation weighting. The partitioned strategy described in Section 2.4.2 is applied at each time step: the equilibrium problem is solved first with all history variables frozen, and the constitutive state is advanced afterward. The equilibrium problem is solved by Newton–Raphson iteration:

$$\mathbf{J}\,\Delta\mathbf{u} = -\mathbf{F}, \qquad \mathbf{u} \leftarrow \mathbf{u} + \omega\,\Delta\mathbf{u}, \tag{28}$$

where $\mathbf{J} = \partial\mathbf{F}/\partial\mathbf{u}$ is obtained by automatic differentiation [63] of the variational form and $\omega \in [\omega_{\text{min}}, 1]$ is a step length determined by an Armijo backtracking line search [92]. Convergence is declared when $\|\mathbf{F}\| < \text{tol}_{\text{abs}}$ or $\|\mathbf{F}\|/\|\mathbf{F}_0\| < \text{tol}_{\text{rel}}$.

The system size remains constant throughout the simulation. Degrees of freedom belonging to unborn elements ($t < t_{\text{b}}^e$) are pinned to zero by replacing the corresponding Jacobian rows and columns with identity constraints and setting the residual entries to zero. When an element transitions from inactive to active, its displacement is initialized from the deformation state of the supporting element in the layer below, identified as the element in the preceding layer whose centroid is closest to the current element's centroid in the build direction. Elements in the first deposited layer, or elements with no active neighbor below, are initialized to zero displacement.

After each converged equilibrium step, the constitutive state is advanced in two separate updates. First, the viscoplastic strain $\boldsymbol{\varepsilon}^{vp}$ is integrated via the substepping procedure described in Section 2.4.2, restricted to cells that are actively yielding. Second, the damage history variable D_{max} is updated by evaluating the damage on all inter-layer facets from the current displacement field. Both quantities are carried forward to the next time step. The complete procedure is formalized in Algorithm 1.

Algorithm 1 Partitioned time-stepping procedure.

Require: Mesh $\mathcal{T}_h$ with facet classification, birth times $\{t_{\rm b}^e\}$, parameters (Tables 1–2), user-specified number of time steps $N_{\rm steps}$
Set: $\Delta t \leftarrow t_{\rm b}^{\max}/N_{\rm steps}$ ▷ Uniform subdivision of total deposition time
Output: $\mathbf{u}^n$, $\boldsymbol{\varepsilon}^{vp,n}$, $D^n_{\max}$ at each time step

Initialize $\mathbf{u} \leftarrow \mathbf{0}$, $\boldsymbol{\varepsilon}^{vp} \leftarrow \mathbf{0}$, $D_{\max} \leftarrow 0$
for each time step $t^{n+1} = t^n + \Delta t$ **do**
  — Domain preparation (Section 2.3) —
  Update activation α^{n+1} via Eq. (3) ▷ Smooth tanh ramp from $\alpha_{\min}$ to 1
  Update E, ν, G, $\sigma_{\rm y}$, η via Eqs. (4)–(7) ▷ Age-dependent properties
  Evaluate $\beta_{\rm bond}$ for newly contacted inter-layer facets via Eq. (12) ▷ Frozen once both layers active
  Copy $\mathbf{u}_e$ from supporting element below for each newly active element e ▷ Conform to deformed substrate
  Pin DOFs of unborn elements: $\mathbf{u}_i = 0$, $J_{ii} = 1$, $F_i = 0$ ▷ Constant system size

  — Equilibrium solve (Section 2.4.2): $\boldsymbol{\varepsilon}^{vp,n}$ and $D^n_{\max}$ frozen —
  $\mathbf{u}^{(0)} \leftarrow \mathbf{u}^n$ ▷ Previous converged state as initial guess
  for $k = 0, 1, 2, \ldots$ **do**
    Assemble $\mathbf{F}(\mathbf{u}^{(k)})$ and $\mathbf{J}(\mathbf{u}^{(k)})$ ▷ Eq. (21); $\mathbf{J}$ via automatic differentiation
    Solve $\mathbf{J}\,\Delta\mathbf{u} = -\mathbf{F}$
    Armijo line search: find $\omega \in [\omega_{\min}, 1]$ ▷ Halve ω until sufficient decrease
    $\mathbf{u}^{(k+1)} \leftarrow \mathbf{u}^{(k)} + \omega\,\Delta\mathbf{u}$ ▷ Damped Newton update
    break if $\|\mathbf{F}\| < \mathrm{tol}_{\rm abs}$ or $\|\mathbf{F}\|/\|\mathbf{F}_0\| < \mathrm{tol}_{\rm rel}$
  end for
  $\mathbf{u}^{n+1} \leftarrow \mathbf{u}^{(k+1)}$

  — Viscoplastic strain update (Section 2.4.2): yielding cells only —
  for each cell e with $f(\boldsymbol{\sigma}_e^{n+1}) > 0$ **do** ▷ Eq. (9); skip elastic cells
    $n_{\rm sub} \leftarrow \lceil \Delta t \cdot E_e/\eta_e \rceil$ ▷ Substeps for explicit stability: $\Delta t_{\rm sub} \le \eta_e/E_e$
    for $j = 1, \ldots, n_{\rm sub}$ **do**
      $\boldsymbol{\varepsilon}_e^{vp} \leftarrow \boldsymbol{\varepsilon}_e^{vp} + \dfrac{\Delta t}{n_{\rm sub}}\,\dot{\boldsymbol{\varepsilon}}^{vp}(\boldsymbol{\sigma}_e^{n+1}, t_{\rm age})$ ▷ Perzyna flow rule, Eq. (10)
    end for
  end for

  — Damage history update (Section 2.4.3) —
  for each inter-layer facet **do**
    $D \leftarrow$ Eq. (17) evaluated at $\mathbf{u}^{n+1}$ ▷ Mixed-mode exponential damage
    $D_{\max} \leftarrow \max(D, D_{\max})$ ▷ Irreversibility: damage can only grow
  end for
end for

3. Verification

This section verifies the numerical implementation through a sequence of tests that isolate individual components before combining them in coupled problems. Tests 1–4 validate the linear DG discretization (patch test and MMS convergence), the cohesive traction law evaluated from the production UFL expressions, and the viscoplastic constitutive time integrator, respectively. Test 5 then verifies the full coupled system—bulk elasticity, SIPG coupling, Nitsche boundary conditions, gravitational body force, and Newton's method—against a closed-form self-weight solution, providing an end-to-end check of the adopted unit system; a sequential activation variant of the same problem verifies element birth and DOF pinning. The final benchmark (Test 6) tests the nonlinear cohesive response within a solved global equilibrium problem. When the mesh is cubic it is denoted by n^3; otherwise the full dimensions are reported explicitly. Throughout, "round-off-level agreement" denotes relative errors on the order of 10^{-14}–10^{-15}.

3.1. Patch test

The patch test [93, 94] verifies that a uniform stress state, equivalently a linear displacement field, is reproduced exactly by the discrete approximation. For standard continuous Galerkin methods this property is guaranteed by the shared-node topology, but for the present DG formulation it must be verified explicitly: the SIPG consistency, symmetry, and penalty terms must cancel inter-element fluxes exactly, and the Nitsche boundary terms must enforce the prescribed displacement without introducing spurious residual forces.

The test domain is a $10\times10\times5$ mm block discretized with hexahedral elements into two layers, producing an inter-layer cohesive interface at the mid-plane and intra-layer SIPG faces within each layer (Fig. 6a). Non-homogeneous Dirichlet conditions $\mathbf{u} = \mathbf{g}$ are imposed on all six faces using Nitsche's method, where $\mathbf{g}(\mathbf{x})$ is a prescribed linear displacement field. The material is linear elastic ($E = 1000$ MPa, $\nu = 0.3$), no body force is applied, all elements are fully active ($\alpha = 1$), and both viscoplasticity and cohesive damage are suppressed.

Three load cases are considered: (i) uniaxial tension ($\varepsilon_{xx} = \varepsilon_0$, $\varepsilon_{yy} = \varepsilon_{zz} = -\nu\varepsilon_0$), (ii) pure shear ($\varepsilon_{xy} = \varepsilon_0/2$), and (iii) hydrostatic strain ($\varepsilon_{xx} = \varepsilon_{yy} = \varepsilon_{zz} = \varepsilon_0$), with $\varepsilon_0 = 10^{-3}$. Together these span the normal, shear, and volumetric components of the stress tensor. Each case is solved on four meshes (2^3, 4^3, 6^3, 8^3 elements).

Because the exact solution is linear and therefore lies in the DG1 trial space, the numerical solution should be exact up to round-off. Table 3 confirms this: the maximum L^∞ relative error over all three load cases ranges from 2×10^{-15} to 1.4×10^{-14}. The slight increase with refinement (Fig. 6b) is consistent with accumulated floating-point round-off over a larger number of element contributions.

The patch test confirms that the SIPG intra-layer terms, the cohesive inter-layer penalty, and the Nitsche boundary conditions are consistently implemented. This is a necessary condition for the optimal convergence rates demonstrated in Section 3.2.

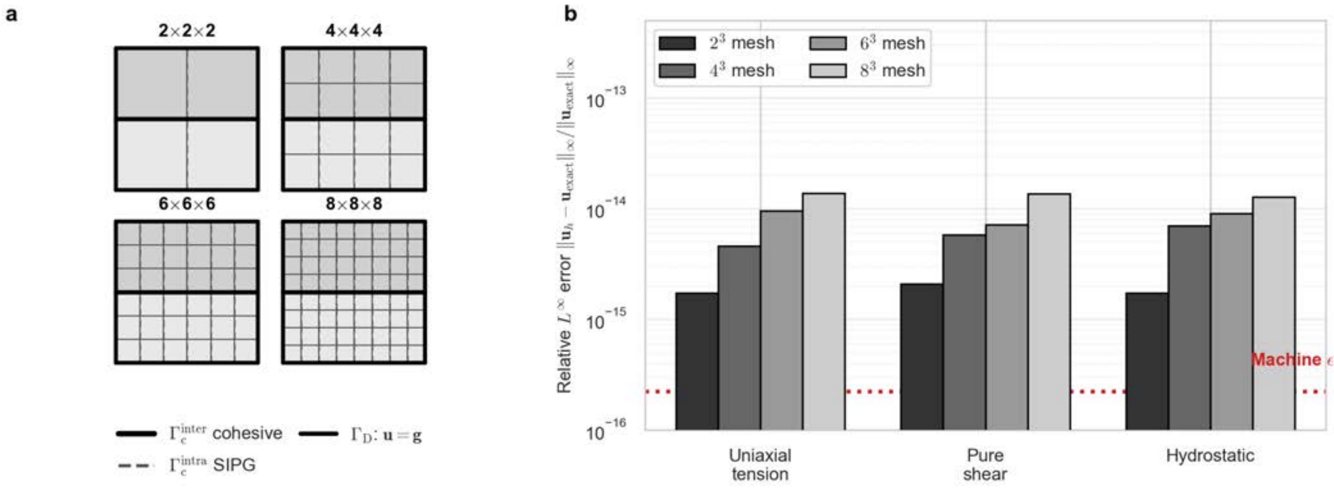

Figure 6: DG elastic patch test. (a) Two-layer meshes at four refinement levels. (b) L^∞ relative displacement error for the three load cases; the dashed line denotes ϵ_{mach}.

Table 3: DG elastic patch test: maximum L^∞ relative error across the three load cases.

Mesh	Newton iter.	max $\|\mathbf{u}_h - \mathbf{u}_{\text{exact}}\|_\infty / \|\mathbf{u}_{\text{exact}}\|_\infty$
2^3	1	2.08×10^{-15}
4^3	1	7.03×10^{-15}
6^3	1	9.54×10^{-15}
8^3	1	1.37×10^{-14}

3.2. Spatial convergence via the method of manufactured solutions

The patch test confirms that a constant stress state is exactly representable, but does not characterize the rate at which the discretization error decreases with mesh refinement. To establish this, the method of manufactured solutions (MMS) [95] is applied: a smooth displacement field is chosen as the exact solution, the corresponding body force is derived analytically, and the computed solution is compared against the known answer on a sequence of refined meshes.

The manufactured displacement field is the smooth trigonometric vector field

$$\mathbf{u}_{\text{exact}}(\mathbf{x}) = \begin{pmatrix} \sin(\pi x)\ \cos(\pi y)\ \cos(\pi z) \\ \cos(\pi x)\ \sin(\pi y)\ \cos(\pi z) \\ \cos(\pi x)\ \cos(\pi y)\ \sin(\pi z) \end{pmatrix}, \tag{29}$$

on the unit cube $[0, 1]^3$. This field is non-polynomial and couples all three displacement components with coupled spatial variation, ensuring that the convergence study is not biased toward any particular direction. It is not divergence-free, so both the volumetric (λ) and deviatoric (μ) parts of the stress are engaged. Symbolic differentiation gives the required body force as

$$\mathbf{f} = \frac{3\pi^2}{L^2}\,(\lambda + 2\mu)\,\mathbf{u}_{\text{exact}}, \tag{30}$$

with $L = 1$ mm. The reduction to a single prefactor follows from the cyclic symmetry of the displacement field. Material properties and boundary treatment are the same as in Section 3.1, with all interior facets treated as intra-layer SIPG faces and non-homogeneous Nitsche conditions imposed on all boundary faces.

Fifteen meshes are used, from $n = 2$ to $n = 16$ elements per side. Figure 7 and Table 4 show that the L^2 error decreases at a mean rate of 2.02, matching the theoretical $O(h^2)$ rate for $\mathbb{Q}^1$ DG elements, while the broken H^1 semi-norm decreases at 1.00, matching $O(h)$ [43]. Both rates are established from $n = 4$ onward and remain stable on all finer meshes. These results verify that the SIPG interior penalty terms and the Nitsche boundary conditions are correctly scaled and that the overall DG discretization achieves optimal convergence for smooth solutions.

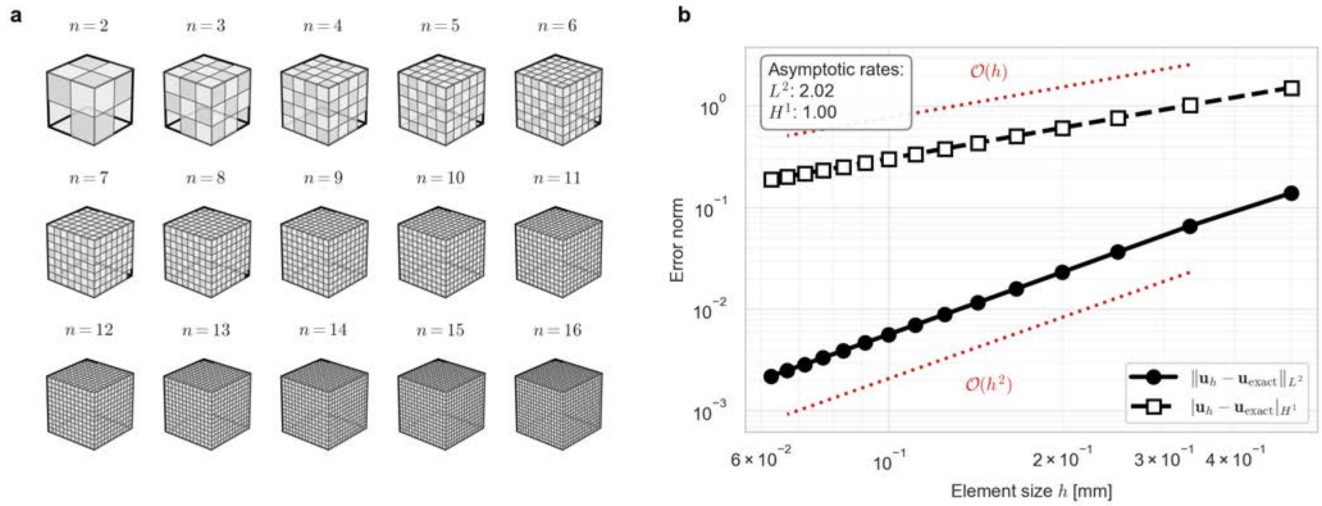

Figure 7: MMS spatial convergence. (a) Unit-cube meshes used in the 15-level refinement study ($n = 2, \ldots, 16$). (b) L^2 error at $O(h^2)$ and broken H^1 semi-norm at $O(h)$; dashed lines indicate reference slopes.

Table 4: MMS spatial convergence. Selected levels from the 15-level study; the first two levels ($n = 2, 3$) are pre-asymptotic.

n	h	$\|e\|_{L^2}$	Rate	$\lvert e\rvert_{H^1}$	Rate
2	0.5000	1.39×10^{-1}	—	1.51×10^{0}	—
4	0.2500	3.64×10^{-2}	2.05	7.61×10^{-1}	1.01
6	0.1667	1.59×10^{-2}	2.04	5.05×10^{-1}	1.01
8	0.1250	8.84×10^{-3}	2.03	3.78×10^{-1}	1.00
10	0.1000	5.63×10^{-3}	2.02	3.03×10^{-1}	1.00
12	0.0833	3.90×10^{-3}	2.01	2.52×10^{-1}	1.00
14	0.0714	2.86×10^{-3}	2.01	2.16×10^{-1}	1.00
16	0.0625	2.19×10^{-3}	2.01	1.89×10^{-1}	1.00

3.3. *Cohesive traction–separation law verification*

The DG formulation couples adjacent layers exclusively through the cohesive traction $\mathbf{T}_c$ (Eqs. (18)–(20)), so the accuracy of the interface response directly governs the fidelity of delamination predictions. This test verifies that the UFL implementation of the exponential cohesive damage law reproduces the analytical traction–separation relation to round-off level.

The test domain is a two-element hexahedral mesh ($1 \times 1 \times 1$ mm) split at $z = 0.5$ mm, with the shared facet classified as an inter-layer cohesive interface. A uniform normal opening δ_n is prescribed by rigidly displacing the two elements in opposite directions, producing a displacement jump $[\![\mathbf{u}]\!] = \delta_n \mathbf{n}$ with zero tangential component. The cohesive traction is evaluated by integrating the same UFL expression used in the production weak form (Eq. (23)) over the cohesive facet and dividing by the facet area. For pure mode I, with $\boldsymbol{\delta}_t = \mathbf{0}$ and bond quality $\beta_{bond} = 1$, the analytical response of Eqs. (17)–(18) reduces to

$$T_n(\delta_n) = [(1 - D) K_n + D\, r\, K_n]\, \delta_n, \qquad D = 1 - \exp\left(-\frac{\delta_n^2}{\delta_0^2}\right), \tag{31}$$

where $\delta_0 = \sqrt{2\, G_{Ic}/K_n}$ is the characteristic opening, $K_n = \sigma_c^2/(2\, G_{Ic})$ is the initial interface stiffness, and $r = 0.05$ is the residual stiffness ratio. Because $r > 0$, the traction does not decay to zero for large openings but approaches a residual branch $T_n \sim r\, K_n\, \delta_n$—an intentional regularization that prevents the Jacobian from becoming singular at full damage ($D = 1$), at the cost of unbounded energy dissipation for arbitrarily large separations. The fracture energy G_{Ic} therefore represents the energy dissipated by the primary softening branch, not the total energy for complete separation. Setting $dT_n/d\delta_n = 0$ and solving numerically for $r = 0.05$ gives a peak traction of $0.444\, \sigma_c$ at $\delta_n = 0.739\, \delta_0$, which is 3.4% higher than the $r = 0$ value of $\sigma_c/\sqrt{2e} \approx 0.429\, \sigma_c$. The parameter σ_c thus serves as a scale for the interface stiffness rather than the literal peak traction of the law.

Five cases are tested. Cases (i)–(iii) verify the law in pure mode I across different stiffness–toughness combinations with full bond quality ($\beta_{bond} = 1$): (i) $\sigma_c = 5$ MPa, $G_{Ic} = 0.08$ N/mm; (ii) $\sigma_c = 3$ MPa, $G_{Ic} = 0.08$ N/mm; (iii) $\sigma_c = 5$ MPa, $G_{Ic} = 0.20$ N/mm.

Case (iv) emulates reduced bond quality $\beta_{\mathrm{bond}} = 0.5$ by halving the effective strength and toughness, giving $\sigma_c = 2.5$ MPa and $G_{\mathrm{Ic}} = 0.04$ N/mm in the verification run. Each pure-mode case is evaluated from $\delta_n = 0$ to $5\,\delta_0$. Case (v) activates mixed-mode coupling by prescribing simultaneous normal and tangential jumps with $\delta_t/\delta_n = 1$, engaging the coupled damage measure $D = 1 - \exp(-\delta_n^2/\delta_{0n}^2 - \delta_t^2/\delta_{0t}^2)$ with $\sigma_c = 5$ MPa, $G_{\mathrm{Ic}} = 0.08$ N/mm, $G_{\mathrm{IIc}} = 0.14$ N/mm, and $\tau_c = \sigma_c/\sqrt{3}$.

Figure 8 summarizes the results. The computed traction–separation curves for the four mode I cases (Fig. 8b) are indistinguishable from the analytical predictions, as are the normal and tangential components of the mixed-mode response (Fig. 8c). Maximum relative errors remain at or below 1.2×10^{-15} in all five cases, confirming that the UFL expressions for the exponential damage function, the normal–tangential decomposition, and the damage-degraded traction law are implemented correctly.

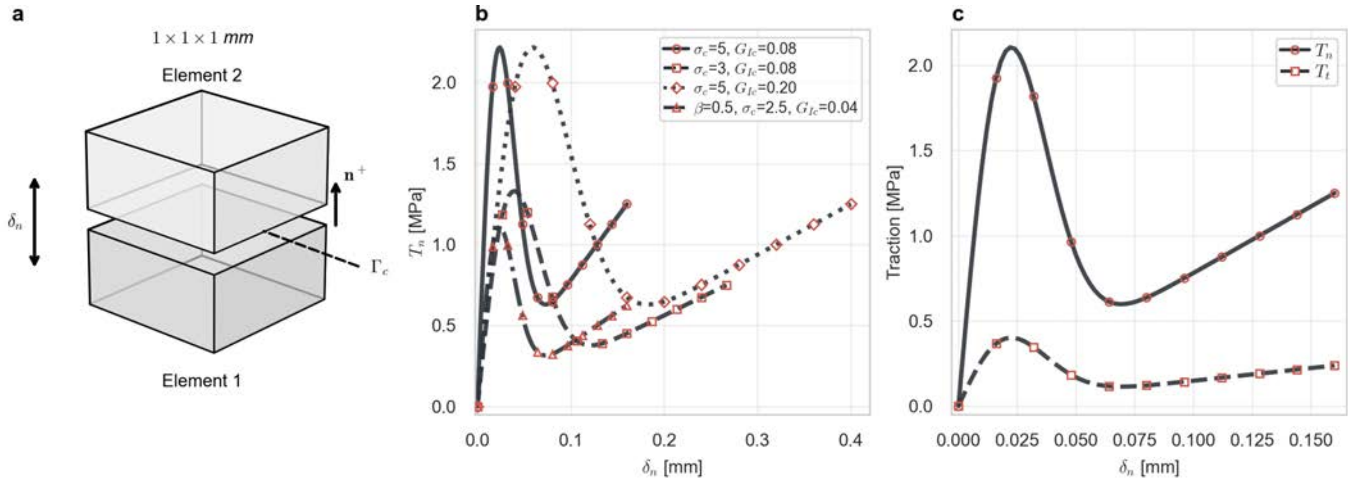

Figure 8: Cohesive traction–separation verification. (a) Two-element setup with prescribed normal opening across Γ_c. (b) Mode I: analytical curves (lines) and numerical results (markers) for four parameter sets. (c) Mixed mode ($\delta_t = \delta_n$): normal and tangential traction components. All relative errors are at or below 1.2×10^{-15}.

3.4. Viscoplastic time integration convergence

This test verifies both the forward-Euler Perzyna integrator (Eq. (10)) and the production substepping rule used to maintain stability when the macro time step exceeds the critical limit.

A single material point is subjected to monotonic uniaxial strain $\varepsilon_{11}(t) = \dot{\varepsilon}\,t$ with $\dot{\varepsilon} = 10^{-3}$ s^{-1} over $T = 10$ s, corresponding to a final strain of 1%. The material parameters are $E = 1000$ MPa, $\nu = 0.3$, $\sigma_y = 2.0$ MPa, and $\eta = 10.0$ MPa·s, placing the yield point at 0.2% strain so that approximately 80% of the loading history occurs in the viscoplastic regime. The explicit forward-Euler scheme is conditionally stable with critical time step $\Delta t_{\mathrm{crit}} = \eta/E = 0.01$ s[85]; time steps exceeding this limit cause exponential error growth in the absence of substepping. A reference solution is computed with $N_{\mathrm{ref}} = 10^5$ time steps.

Part A: Raw integrator ($\Delta t \le \eta/E$). Eight time-step counts within the stable regime are tested, spanning $\Delta t = 0.01$ s to 0.001 s, with no substepping. The stress error decreases at a mean rate of 1.04, confirming first-order $O(\Delta t)$ convergence (Fig. 9, Table 5).

Part B: Substepped algorithm ($\Delta t > \eta/E$). In production simulations, the macro step may exceed η/E because time stepping is tied to the deposition schedule rather than the local constitutive stability limit. The integrator therefore subdivides each macro step into $n_{\mathrm{sub}} = \lceil \Delta t/(\eta/E) \rceil$ substeps of size $\Delta t_{\mathrm{sub}} \le \eta/E$. Eight macro step counts are tested, from $\Delta t = 2.0$ s ($200 \times \Delta t_{\mathrm{crit}}$) down to 0.01 s.

With substepping, the error remains bounded at $\sim 1.4 \times 10^{-2}$ MPa even at $200\,\Delta t_{\mathrm{crit}}$. This plateau occurs because the effective integration step is the substep size, which remains $\approx \eta/E$ regardless of the macro step; increasing Δt adds more substeps but does not change Δt_{sub}, so the accumulated error saturates. As Δt approaches η/E, $n_{\mathrm{sub}} \to 1$ and the error smoothly joins the raw-integrator regime, confirming a seamless transition between the two cases.

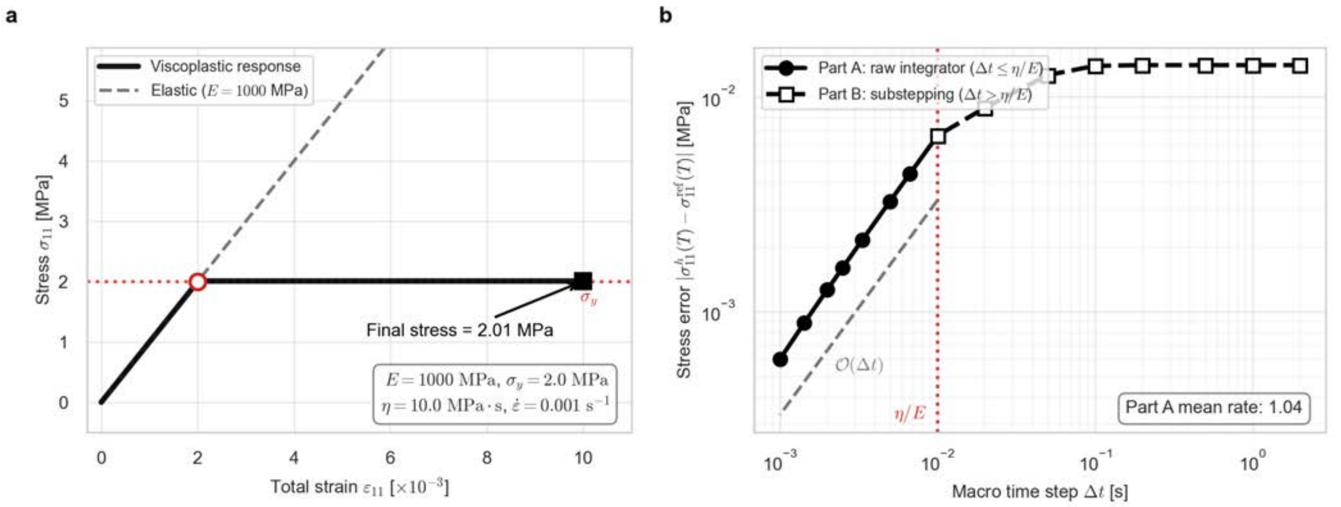

Figure 9: Perzyna viscoplastic temporal convergence. (a) Stress–strain response; $\sigma_{\mathrm{ref}} = 4.68$ MPa at 1% strain. (b) Stress error at $t = T$. Part A (circles): $O(\Delta t)$ within the stable regime. Part B (squares): substepping for $\Delta t > \eta/E$; the vertical dotted line marks η/E.

Table 5: Perzyna viscoplastic temporal convergence. Selected step sizes from the eight-level studies in Parts A and B.

Part A: Raw integrator ($\Delta t \le \eta/E$)				
N	Δt [s]	$\lvert\sigma^h_{11} - \sigma^{\mathrm{ref}}_{11}\rvert$ [MPa]	Rate	n_{sub}
1000	0.0100	6.60×10^{-3}	—	1
2000	0.0050	3.27×10^{-3}	1.02	1
4000	0.0025	1.60×10^{-3}	1.04	1
7000	0.0014	8.86×10^{-4}	1.06	1
10000	0.0010	6.00×10^{-4}	1.09	1
Part B: Substepped algorithm ($\Delta t > \eta/E$)				
5	2.0000	1.41×10^{-2}	—	200
10	1.0000	1.41×10^{-2}	—	100
50	0.2000	1.41×10^{-2}	—	20
200	0.0500	1.26×10^{-2}	—	5
500	0.0200	8.91×10^{-3}	—	2
1000	0.0100	6.60×10^{-3}	—	1

3.5. *Self-weight elastic column*

The preceding tests verify individual components in isolation. This benchmark verifies the full coupled system—bulk elasticity, SIPG coupling, Nitsche boundary conditions, gravitational body force, and Newton's method—against a closed-form solution, and also provides an end-to-end check of consistency in the adopted unit system (mm, MPa, N·s^2/mm^4).

The domain is a vertical column of height $H = 100$ mm with a 10×10 mm cross-section, discretized with hexahedral DG1 elements. The material is linear elastic ($E = 1000$ MPa, $\nu = 0.3$) with density $\rho = 2250$ kg/m^3 ($= 2.25 \times 10^{-9}$ N·s^2/mm^4 in consistent units) and $g = 9810$ mm/s^2. To obtain a closed-form reference, the column is treated as laterally confined: Poisson expansion is suppressed ($u_x = u_y = 0$) so that the vertical displacement depends only on z through the oedometric modulus $\lambda + 2\mu$,

$$u_z(z) = -\frac{\rho g}{\lambda + 2\mu}\left(H z - \tfrac{z^2}{2}\right), \qquad u_x = u_y = 0. \tag{32}$$

This solution is imposed on every boundary face via Nitsche's method, so the only error is the volumetric discretization error. Because u_z is quadratic in z, it lies outside the DG1 space and should converge under mesh refinement. Fifteen refinement levels are tested, from $n = 2$ to $n = 16$ elements in the vertical direction, with $n_z = n$ and $n_x = n_y = \max(2, \lfloor n/2 \rfloor)$ so that the cross-section is refined proportionally while remaining sufficiently resolved on coarse meshes.

The oedometric modulus for the chosen parameters is $\lambda + 2\mu = 1346.2$ MPa, giving an exact tip displacement of $u_z(H) = -8.20 \times 10^{-5}$ mm. Figure 10a shows the 15 column meshes in isometric view, arranged in a grid from $n = 2$ (left) to $n = 16$ (right). The convergence plot (Fig. 10b) displays the relative L^2 displacement error (filled circles, solid line) and the relative broken H^1 semi-norm error (open squares, dashed line) against element size h_z on log–log axes, together with reference slopes of $O(h^2)$ and $O(h)$ (red dotted lines).

Table 6 reports selected levels. The L^2 error decreases from 3.1×10^{-2} on the coarsest mesh to 4.4×10^{-4} on the finest, a 71-fold reduction at a mean asymptotic rate of 2.04 (from $n = 4$ onward). The broken H^1 semi-norm decreases from 5.4×10^{-1} to 3.2×10^{-2}, a 17-fold reduction at a mean rate of 1.12. Both are consistent with the theoretical $O(h^2)$ and $O(h)$ rates for

DG1 elements [43]. The mild oscillation in the H^1 rate visible in the table and the slight scatter of the open squares about the reference slope in Fig. 10b are attributed to changing element aspect ratios introduced by the proportional cross-section refinement. This test confirms that the gravitational body force is correctly assembled and that the full DG formulation achieves optimal convergence for a physically meaningful loading scenario.

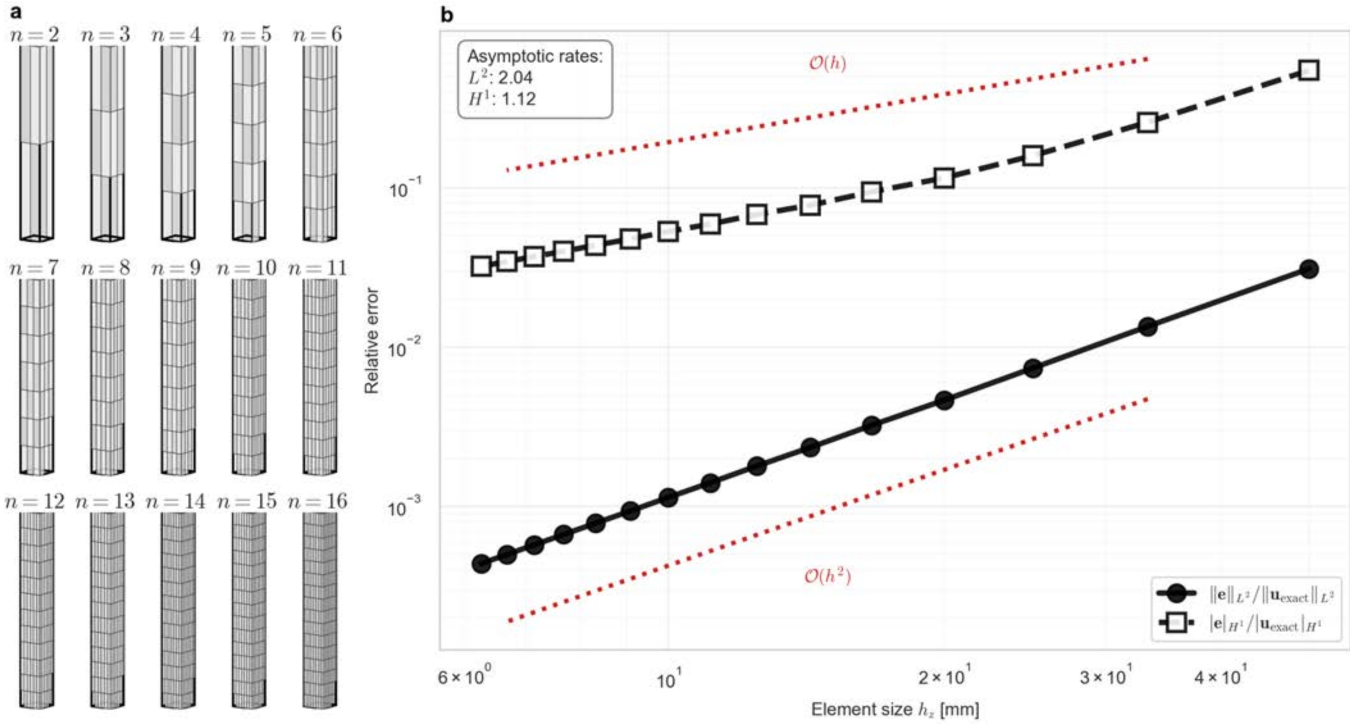

Figure 10: Self-weight elastic column. (a) Isometric views of the 15 column meshes (n = 2 to 16), with $n_z = n$ and $n_x = n_y = \max(2, \lfloor n/2 \rfloor)$. (b) Relative L^2 displacement error (filled circles) and relative broken H^1 semi-norm error (open squares) versus element size h_z; red dotted lines indicate the theoretical $O(h^2)$ and $O(h)$ reference slopes. The inset text box reports asymptotic rates computed from n = 4 onward.

Table 6: Self-weight column convergence. Selected levels from the 15-level study.

n	h_z [mm]	$\|\|e\|\|_{L^2}/\|\|u\|\|_{L^2}$	Rate	$\|e\|_{H^1}/\|u\|_{H^1}$	Rate
2	50.00	3.10×10^{-2}	—	5.45×10^{-1}	—
4	25.00	7.37×10^{-3}	2.09	1.59×10^{-1}	1.67
6	16.67	3.22×10^{-3}	1.99	9.41×10^{-2}	1.11
8	12.50	1.79×10^{-3}	2.00	6.79×10^{-2}	1.00
10	10.00	1.14×10^{-3}	2.02	5.30×10^{-2}	1.03
12	8.33	7.83×10^{-4}	2.02	4.35×10^{-2}	1.02
14	7.14	5.72×10^{-4}	2.02	3.70×10^{-2}	1.02
16	6.25	4.37×10^{-4}	2.02	3.21×10^{-2}	1.02

The same column problem also serves to verify the element activation mechanism. Eight layers are activated sequentially from bottom to top (Fig. 11) using the tanh birth function (Eq. (3)) with sharpness $s = 5$ and $\alpha_{\min} = 10^{-10}$, while degrees of freedom associated with unborn elements are pinned to zero. After all layers are active, the resulting displacement field is compared with the corresponding all-at-once solution under two boundary configurations. In Variant A the analytical field $\mathbf{u}_{\text{exact}}$ is prescribed on all faces, making the final linear system independent of activation order; the relative displacement difference is 5.8×10^{-15}, i.e. at round-off level. In Variant B, Nitsche conditions are imposed only at $z = 0$ and the lateral faces are traction-free, representing the physically meaningful case; the relative difference is 8.5×10^{-13}, still negligible for the present verification purpose but no longer at round-off level. In both variants, unborn DOFs remain exactly zero at every intermediate step. The sequential activation solves are also markedly more demanding than the all-at-once static solve: in the recorded runs they use the full 50-iteration Newton budget while the activation front is still moving, then collapse to a single Newton step once all layers are active. These results confirm correct implementation of DOF pinning, the $\min(\alpha^+, \alpha^-)$ facet convention, and the interaction of activation with the Nitsche boundary terms.

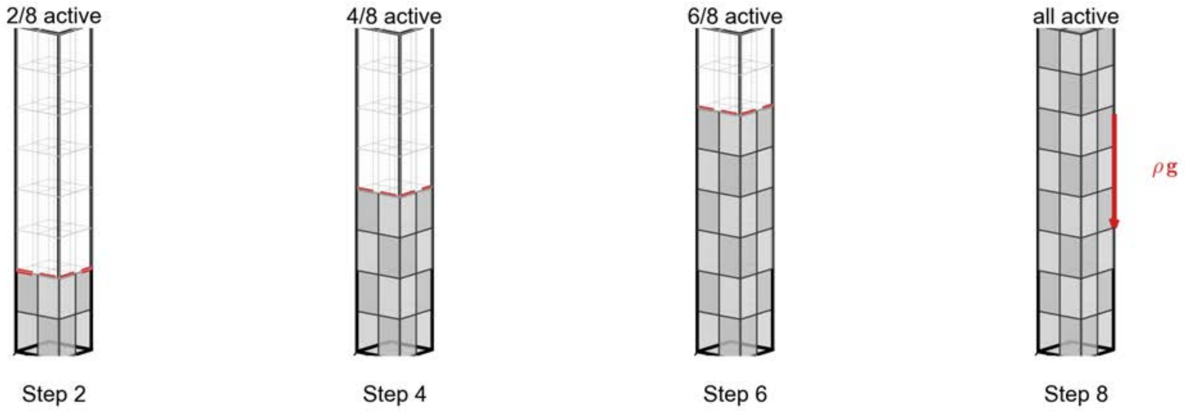

Figure 11: Sequential element activation. Four snapshots show progressive layer activation on a $2 \times 2 \times 8$ mesh. After all eight layers are active, the final displacement field differs from the all-at-once solution by 5.8×10^{-15} in Variant A and 8.5×10^{-13} in Variant B.

3.6. Coupled cohesive equilibrium benchmark

The preceding cohesive verification (Section 3.3) confirms that the UFL expressions reproduce the analytical traction–separation law pointwise. The final test verifies that the cohesive interface functions correctly within a solved equilibrium problem, where interface tractions and bulk stresses interact through the global Newton iteration.

The benchmark is a butt joint of two blocks ($L = 2$ mm, $W = H = 2$ mm) connected by a vertical cohesive interface Γ_c at $x = L/2$ (Fig. 12a). The left block is clamped using Nitsche's method ($\mathbf{u} = \mathbf{0}$), and a prescribed axial displacement δ is applied at $x = L$. The bulk material is linear elastic ($E = 1000$ MPa, $\nu = 0$). Setting the Poisson ratio to zero decouples the axial and transverse directions, so that the exact 3D solution reduces to a one-dimensional two-bar-in-series model with an intermediate cohesive spring. This makes the full analytical force–displacement curve available for direct comparison at every load step—not just the initial stiffness. The cohesive parameters are $\sigma_c = 2.0$ MPa, $G_{Ic} = 0.02$ N/mm, $G_{IIc} = 0.04$ N/mm, and $r = 0.01$. This geometry ensures that the entire axial load is transferred through the cohesive interface, directly exercising the damage mechanics.

Analytical solution. At each prescribed displacement δ, force equilibrium and compatibility require

$$\delta = \frac{T_n(\delta_n)\, L}{E} + \delta_n, \qquad F = T_n(\delta_n)\, A, \tag{33}$$

where $T_n(\delta_n)$ is the cohesive traction from Eq. (31), $A = WH$ is the cross-sectional area, and δ_n is the interface opening. This scalar nonlinear equation is solved at each load step by Newton's method to obtain the exact force $F(\delta)$. In the undamaged limit ($D = 0$), the bar stiffness is

$$K_{bar} = \left[\frac{L}{EA} + \frac{1}{K_n A}\right]^{-1} = 333.3 \text{ N/mm},$$

where $K_n = \sigma_c^2/(2\, G_{Ic}) = 100$ MPa/mm.

Numerical results. The applied displacement is increased from $\delta = 0$ to $\delta = 8\,\delta_0 = 0.16$ mm over 40 load steps, where $\delta_0 = \sqrt{2\, G_{Ic}/K_n} = 0.02$ mm. Seven meshes are tested ($n = 2, 3, 4, 5, 6, 7, 10$), with $n_x = \max(4, 2n)$ and $n_y = n_z = \max(2, n)$. Newton's method converges in 1–3 iterations per step, consistent with the Jacobian correctly capturing the cohesive tangent stiffness including the damage-dependent terms.

With $\nu = 0$, the exact displacement field is piecewise linear (constant strain in each block plus a displacement jump at the cohesive interface), which lies entirely within the DG1 trial space. Spatial discretization error is therefore eliminated, and the only remaining discrepancy arises from floating-point accumulation and the weak enforcement of boundary conditions via Nitsche's method. As a result, the maximum relative force error $\max |F_h - F_{ana}| / \max |F_{ana}|$ over the full loading path is mesh-independent, ranging from 4.8×10^{-6} ($n = 2$, $4 \times 2 \times 2$ elements) to 1.6×10^{-5} ($n = 10$, $20 \times 10 \times 10$ elements).

Figure 12a shows the butt-joint geometry with boundary conditions and loading direction. Figure 12b plots the analytical force–displacement curve (solid line) together with the numerical results from the $n = 2$ mesh (open markers); only this single mesh is shown because all seven meshes produce curves that are visually indistinguishable from one another and from the analytical solution. The response is correctly captured through all four phases: the initial linear-elastic rise (slope $K_{bar} = 333.3$ N/mm), the peak force of 3.45 N, the softening branch as cohesive damage develops, and the residual branch governed by $r\, K_n$. The vertical dotted line marks δ_0.

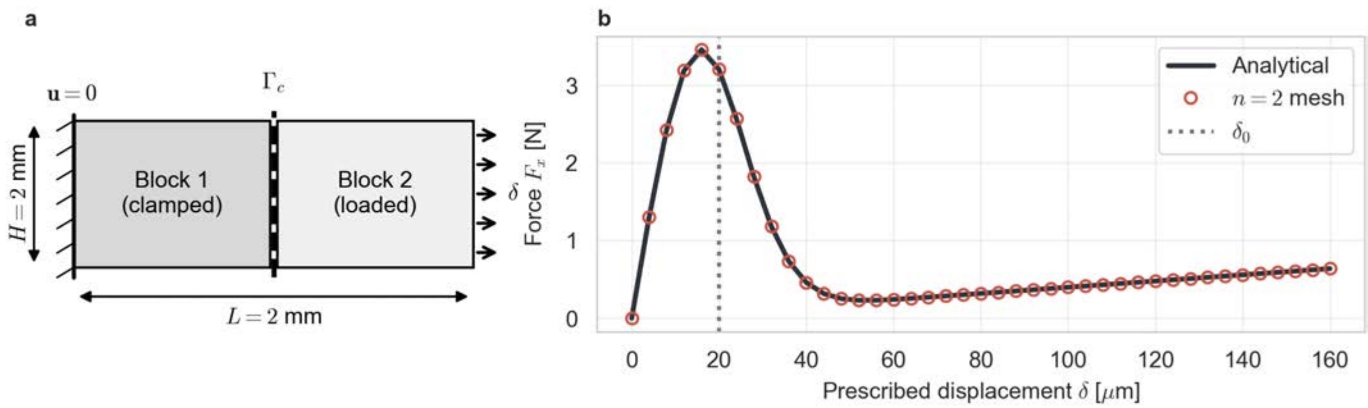

Figure 12: Coupled cohesive equilibrium benchmark. (a) Butt-joint setup: left block clamped, right block pulled by prescribed displacement δ; the vertical dashed line marks the cohesive interface Γ_c. (b) Force–displacement response: analytical solution (solid line) and $n = 2$ numerical results (open markers). All seven meshes ($n = 2$–10) yield indistinguishable curves; the maximum relative force error over the loading path ranges from 4.8×10^{-6} to 1.6×10^{-5}.

4. Validation

This section validates the framework against two experimental prints, fabricated on the same robotic platform with different deposition heads and feedstocks, each isolating one of the two failure mechanisms the formulation is designed to distinguish. The first is a cylinder built along a non-planar toolpath with a single-component (1K) head from a slowly structuring mortar. Its layer interfaces remain in compression and the print fails by plastic collapse of the bulk under accumulating self-weight, so this case tests the bulk viscoplastic model. Because its interfaces never open, the case also admits perfectly bonded reference formulations: a standard continuous Galerkin (CG) discretization and a bonded-DG control. These are introduced here purely for comparison and run against the DG formulation of Section 2.2 to separate the contribution of the cohesive interface from that of the discontinuous discretization and to quantify the computational premium of the interface treatment. The second is a barrel vault printed with a two-component (2K) accelerated system. Its interfaces carry combined tension and shear and the print fails by inter-layer delamination, so this case tests the cohesive interface law. The constitutive parameters of each case are obtained from independent characterization of its own feedstock (Section 4.2).

4.1. Fabrication system and instrumentation

Both specimens were fabricated on the robotic printing platform shown in Figure 13. A KUKA KR120 R2700 HA six-axis industrial robot, mounted on a linear rail serving as a seventh axis, carries an interchangeable deposition head at its end effector. The barrel vault was printed with a 2K extrusion system: material is pumped by a MAI MULTIMIX-3D unit and dosed with accelerator from a separate pump, the two streams combining at the 2K head before extrusion. The cylinder was printed with a 1K head fed by the MAI MULTIMIX-3D unit without inline accelerator.

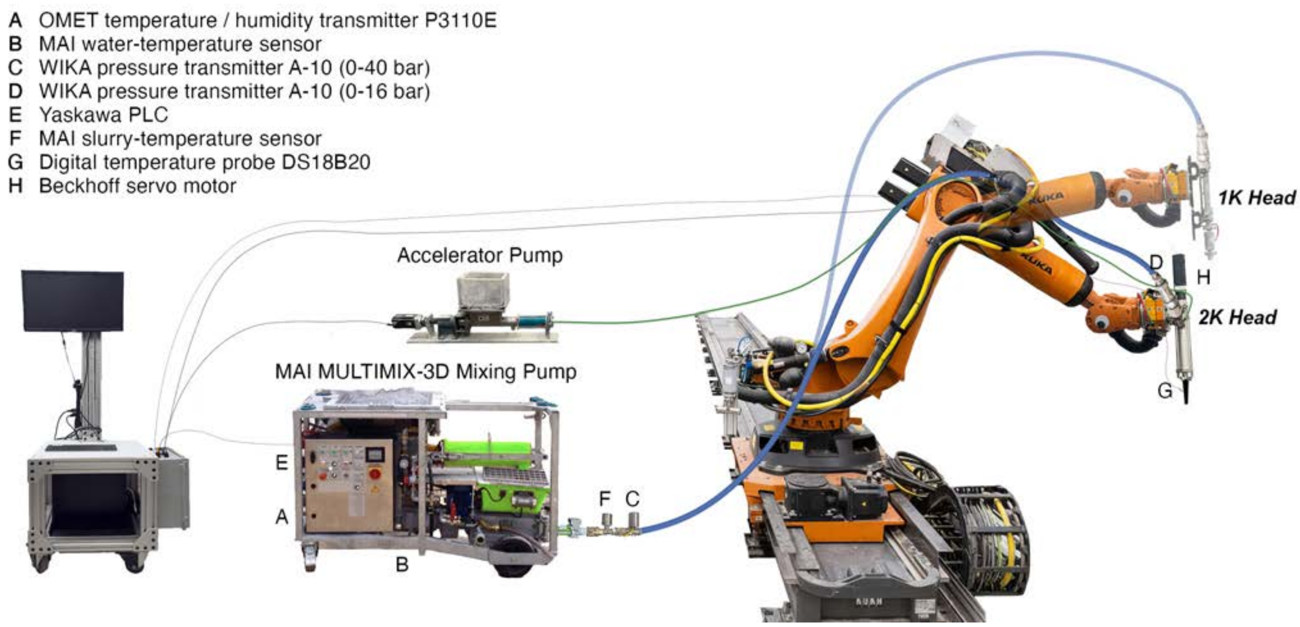

Figure 13: Robotic fabrication platform and integrated sensor suite common to both validation cases. A KUKA KR120 R2700 HA robot on a linear rail deposits material supplied by the MAI MULTIMIX-3D mixing pump through an interchangeable head: the two-component (2K) mixing head used for the barrel vault and the single-component (1K) head used for the cylinder. Labeled instruments: (A) OMET temperature and humidity transmitter P3110E, (B) MAI water-temperature sensor, (C) WIKA A-10 pressure transmitter (0–40 bar), (D) WIKA A-10 pressure transmitter (0–16 bar), (E) Yaskawa PLC, (F) MAI slurry-temperature sensor, (G) DS18B20 digital temperature probe, (H) Beckhoff servo motor.

All simulations reported in this section were performed on an Apple MacBook Pro laptop with an Apple M5 chip and 32 GB of unified memory; the discrete systems were assembled with DOLFINx and solved through PETSc. The barrel-vault simulation ran in parallel with MPI on 4 cores using GMRES preconditioned by GAMG (Section 2.2); the cylinder simulations ran serially with the MUMPS direct solver, so that the three runs of that case differ only in their formulation and their timings are not confounded by parallel partitioning or communication effects. The wall-clock time and the number of active elements at the end of the run for each case are reported at the close of Sections 4.3 and 4.4.

4.2. Material and process parameters

The two cases use different feedstocks. The barrel vault was printed with the Sikacrete-752 3D commercial dry mix accelerated inline with Sika Sigunit L-5601 AF (4 %) and retarded with Sika Plastiment (130 mL/100 kg), documented in the authors' companion lamination-design study [41]. The cylinder was printed with a slowly structuring mortar. The material mix proportions are detailed in Table 7, with a water-to-binder ratio of 0.30, a fly-ash replacement of 55 % of the binder mass, and a superplasticizer dosage of 0.16 % of binder. Each feedstock is characterized through the standard protocols of Table 1; the resulting constitutive parameters are reported per case in Table 8, and the geometries and deposition schedules in Table 9.

For both feedstocks the initial static yield stress $\tau_{0,0}$ is identified from a vane shear test and the critical elastic strain γ_c from oscillatory rheometry in the linear viscoelastic region. The structuration rate A_{thix} is identified from a time-dependent vane test. The shear modulus follows from $G \approx \tau_0/\gamma_c$ (Eq. (5)) and the Young's modulus from the isotropic relation (Eq. (6)). The two materials are an order of magnitude apart in stiffness: the accelerated vault mix gives an initial Young's modulus $E_0 \approx 0.74$ MPa, whereas the unaccelerated cylinder mortar gives $E_0 \approx 0.06$ MPa. The interface fracture energies G_{Ic} and G_{IIc} are not measured directly; they are assigned from published ranges for cementitious interfaces [2, 35, 96]. The same cohesive law and values enter both cases, but they bear on the result only in the vault: the cylinder's interfaces remain in compression and far from decohesion throughout the build, so its predicted response is insensitive to the assigned values.

The effective deposition pressure p_{dep} (Table 9) is the steady-state line pressure during deposition minus the steady-state pressure during free extrusion at the same flow rate (Eq. (13)), obtained on the printing system; it is lower for the cylinder than for the vault. In both cases the substrate yield stress reached over the inter-layer rest time leaves the interface in the strong-bond regime, with a computed bond-quality factor $\beta_{\mathrm{bond}} \approx 1.0$, so the effective interface strengths and fracture energies coincide with their nominal values. The bond-quality factor depends on p_{dep} only through the ratio $\phi = p_{\mathrm{dep}}/\tau_{\mathrm{sub}}$ and saturates as this ratio grows (Eq. (12)); the predicted interface response is therefore insensitive to the precise value of p_{dep} in this regime, and the value becomes influential only as the interface approaches the cold-joint transition.

The two constructs and their deposition schedules are summarized in Table 9. The cylinder is a circular wall of diameter 207 mm and wall width 20 mm, built with the 1K mortar at a nominal layer height of 9 mm and a tool-center-point (TCP) speed of 50 mm s^{-1}; the first eleven layers are imaged and simulated. Its toolpath is sliced non-planarly: the deposition height follows a four-lobed wave whose amplitude grows from ±3 mm at the base to ±16 mm at layer eleven. The barrel vault spans 1200 mm with a rise of 300 mm and an inner radius of 750 mm; it is built with the 2K mix in fifteen layers at a 14 mm layer spacing and a TCP speed of 60 mm s^{-1}.

Table 7: Mix proportions of the cylinder mortar by mass, normalized to total binder mass (OPC plus fly ash = 1).

Constituent	Mass ratio
Ordinary Portland cement	0.45
Fly ash	0.55
Silica sand	0.35
Water	0.30
Superplasticizer	0.0016

Table 8: Characterized constitutive parameters of the two feedstocks.

Parameter	Symbol	Cylinder (1K)	Barrel vault (2K)	Source
Initial static yield stress	$\tau_{0,0}$	210 Pa	2500 Pa	Vane shear test
Structuration rate	A_{thix}	2 Pa s^{-1}	150 Pa s^{-1}	vane test
Critical elastic strain	γ_c	0.01	0.01	Oscillatory rheometry (LVER)
Plastic viscosity	μ_p	6 Pa s	200 Pa s	Rotational rheometry
Initial Young's modulus	E_0	0.06 MPa	0.74 MPa	Derived, Eqs. (5)–(6)
Poisson ratio (fresh)	ν_{fresh}	0.48	0.48	Assumed
Poisson ratio (hardened)	ν_{hard}	0.20	0.20	Assumed
Setting time	t_{set}	3600 s	240 s	Penetration test
Density	ρ	2000 kg m^{-3}	2100 kg m^{-3}	Gravimetric
Mode I fracture energy	G_{Ic}	0.08 N mm^{-1}	0.08 N mm^{-1}	Literature range
Mode II fracture energy	G_{IIc}	0.14 N mm^{-1}	0.14 N mm^{-1}	Literature range

Table 9: Geometry and deposition schedule of the two prints used as simulation inputs.

Parameter	Cylinder	Barrel vault
Construct geometry	diameter 207 mm, non-planar slicing	span 1200 mm, rise 300 mm, radius 750 mm
Layer height	9 mm	14 mm
Number of deposited layers	11	15
TCP speed v_{TCP}	50 mm/s	60 mm/s
Deposition pressure p_{dep}	40 kPa	70 kPa
Print head	single-component (1K)	two-component (2K)

4.3. Bulk collapse of a printed cylinder

This case validates the bulk viscoplastic response against the printed cylinder of Section 4.2. Self-weight loads the inter-layer interfaces in compression, and the unaccelerated 1K mortar structures slowly relative to the deposition rate, so the lower layers yield progressively under the accumulating overburden and the print fails by plastic collapse of the bulk. The comparison proceeds on three fronts: the simulated progression against the recorded print (Figure 14); the per-layer settlement of three formulations, the cohesive DG model and two perfectly bonded references (a continuous Galerkin baseline and a bonded-DG control), against a direct image-based measurement (Figure 15); and the computational cost of the three (Figure 16).

All three formulations share one conformal hexahedral mesh whose layer interfaces follow the measured non-planar slicing wave: 96 cells around the circumference, one through the thickness, and 11 layers (1 056 cells), with heights varying azimuthally between 5.8 and 12.5 mm. Cells are activated sequentially along the deposition path at the measured TCP speed, the base is clamped through Nitsche boundary conditions, all other surfaces are traction-free, and the material parameters are the cylinder column of Table 8.

The CG baseline solves the same physical problem with the displacement in continuous Lagrange elements on the same mesh. Its trial and test space is the continuous subspace of the broken space of Eq. (2),

$$V_h^{\text{CG}} = V_h \cap \left[C^0(\overline{\Omega})\right]^3 = \{\mathbf{v} \in \left[C^0(\overline{\Omega})\right]^3 \ : \ \mathbf{v}\big|_K \in \left[\mathbb{Q}^1(K)\right]^3, \ \forall\, K \in \mathcal{T}_h\}, \tag{34}$$

where $C^0(\overline{\Omega})$ is the space of functions continuous on the closed domain $\overline{\Omega}$ and V_h, $\mathbb{Q}^1(K)$, and $\mathcal{T}_h$ are as defined in Section 2.2. The space contains the same elementwise trilinear functions as V_h and differs only in requiring continuity across element boundaries, which forces the jumps $[\![\mathbf{u}]\!]$ and $[\![\mathbf{v}]\!]$ to vanish on every interior facet. Since the interior-facet terms of the global residual (Eq. (21)) are built from these jumps, the cohesive, SIPG, and stabilization contributions vanish identically, $F_{\text{coh}} = F_{\text{SIP}} = F_{\text{stab}} = 0$: no facet can open or slide, and the layers are perfectly bonded by construction. The CG baseline thus reproduces the continuum idealization of existing part-level buildability models, in which contacting layers merge into a single body. The problem reduces to finding $\mathbf{u} \in V_h^{\text{CG}}$ such that for all $\mathbf{v} \in V_h^{\text{CG}}$

$$F_{\text{bulk}} + F_{\text{BC}} + F_{\text{grav}} = 0, \tag{35}$$

with F_{bulk}, F_{BC}, and F_{grav} the bulk, Nitsche boundary, and gravity terms of Eqs. (22), (26), and (27), each still weighted by the activation function α so the deposition sequence is represented identically across runs.

The bonded-DG control provides a second perfectly bonded reference that keeps the discontinuous discretization rather than replacing it. It retains the broken space V_h and the full interior-facet machinery of the DG run but replaces the cohesive law on the inter-layer facets $\Gamma_{\text{c}}^{\text{inter}}$ with the same symmetric interior-penalty coupling used on the intra-layer facets (Eqs. (24) and (25)). Every interior facet is then bonded: jumps are penalized but admit no traction-free opening or frictional sliding, tying the layers together as in the CG idealization while the displacement remains in the broken space. The two references therefore bracket the cohesive DG result. Sharing the cohesive run's mesh, activation schedule, and solver, the control differs from it only in the inter-layer facet treatment and from CG only in the continuity of the space; the step from CG to the control isolates the discontinuous discretization, and the step from the control to the cohesive run isolates the cohesive interface.

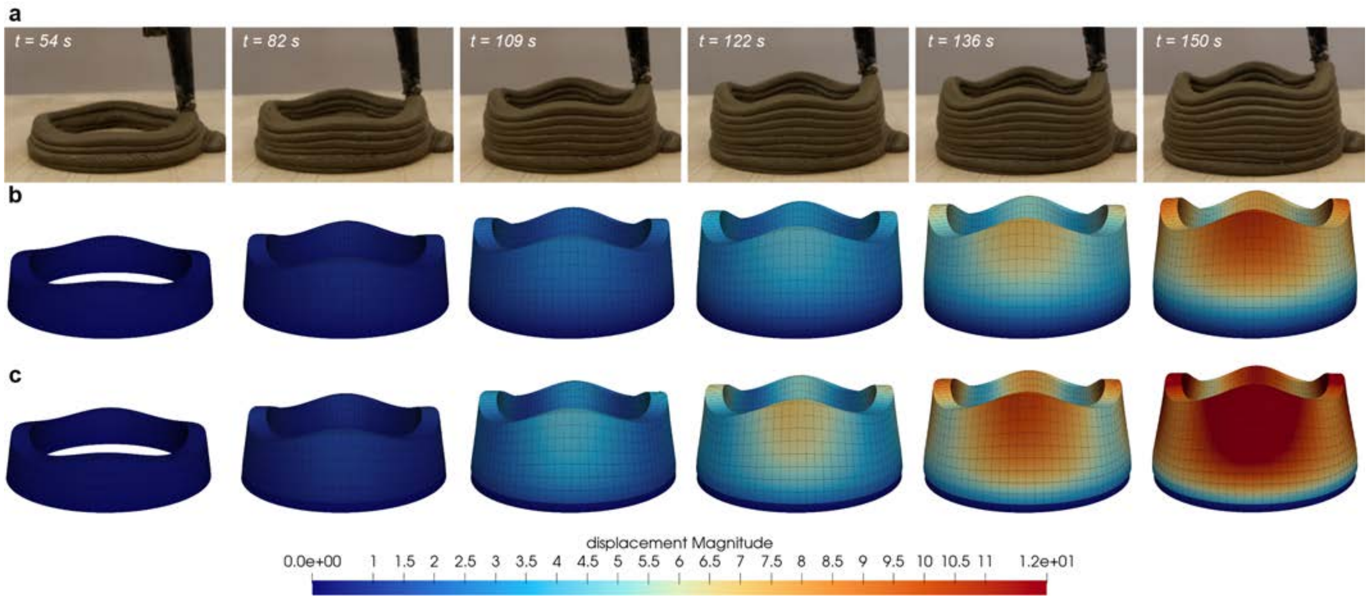

Figure 14: Print progression of the cylinder at the six instants labeled in (a). (a) Photographs of the print. (b) CG and (c) DG simulated front views, warped by the computed displacement and colored by the displacement magnitude $|\mathbf{u}|$ in millimetres; the color range is set per frame, with the corresponding color bar below each snapshot.

Figure 14 compares the recorded print with the CG and cohesive-DG simulations at six common instants; the bonded-DG control, which settles comparably to CG, is carried only in the quantitative comparisons below. Both formulations reproduce the observed progression: the base remains stable, and as the overburden accumulates the lower and middle layers yield, producing the central settlement bowl of the final frames. The deformation concentrates in the body of the stack, while the freshest crest is barely deformed and translates downward on the yielding material below.

The first layer separates the two discretizations most clearly. In the DG run (Figure 14c) the base layer is clamped to the build plate and connected to the stack above only through its cohesive interface; because that interface admits relative displacement, the settling stack does not drag it along, and the base remains nearly undeformed as the layer above settles over it, reproducing the progressive covering of the base bead seen in the photographs. In the CG run (Figure 14b) displacement continuity ties the base layer to the material above, forcing it to compress with the stack, so the localized settlement at the first interface cannot develop.

Figure 15a quantifies the settlement per layer, each simulated layer referenced to the instant it is covered by the next and expressed as a fraction of layer height. Overlaid is a direct image-based measurement, read from the labeled photographs by tracking the visible lower edge of each painted bead from its deposition frame to the final frame, with markers giving the median and interquartile range over roughly 600 image columns. Each simulated curve carries interquartile error bars over the layer's azimuthal samples, so every series uses the same median-and-spread representation.

The cohesive DG model recovers the magnitude and shape of the measured settlement. Its profile rises to a mid-stack peak of 81 % of a layer height at layer six and tapers above it; the measurement forms a broad maximum of 80 % to 88 % over layers four to six, highest at the freshest reliable layer, and both fall below 30 % of a layer height by layer ten. The DG median tracks the measured median to within 4 % of a layer height over layers six to ten, and the measurement lies within the simulated interquartile range from layer five onward, rising just above it only at layer four; this residual underprediction at the freshest reliable layer is consistent with the reference offset noted above, which is largest for the youngest material. The two perfectly bonded formulations underpredict throughout, the CG baseline peaking at 55 % and the bonded-DG control at 49 %.

The bonded-DG control identifies the source of the difference. Its settlement profile nearly coincides with the CG profile, the two differing by less than 7 % of a layer height, so the discontinuous discretization and its penalty-based interface tie add negligible compliance. The cohesive DG run departs from both by up to 34 % of a layer height at mid-stack. The added settlement is thus an interface effect: the cohesive layers, deforming in compression, supply a compliance the perfectly bonded idealizations omit, and this compliance accounts for the measured magnitude. The maximum displacement at the final instant reflects the same ordering, reaching 15 mm in the cohesive DG run against 11 mm for CG and 9 mm for the bonded-DG control.

The DG run additionally reports the interface state, which neither bonded formulation can represent. The maximum inter-layer damage (Figure 15b) stays below 0.23 throughout, rising only in the final frames as the undulating crown bends, and no interface opens: the model identifies the case as governed by bulk deformation, the bulk-side counterpart of the delamination identified with the same interface law in Section 4.4.

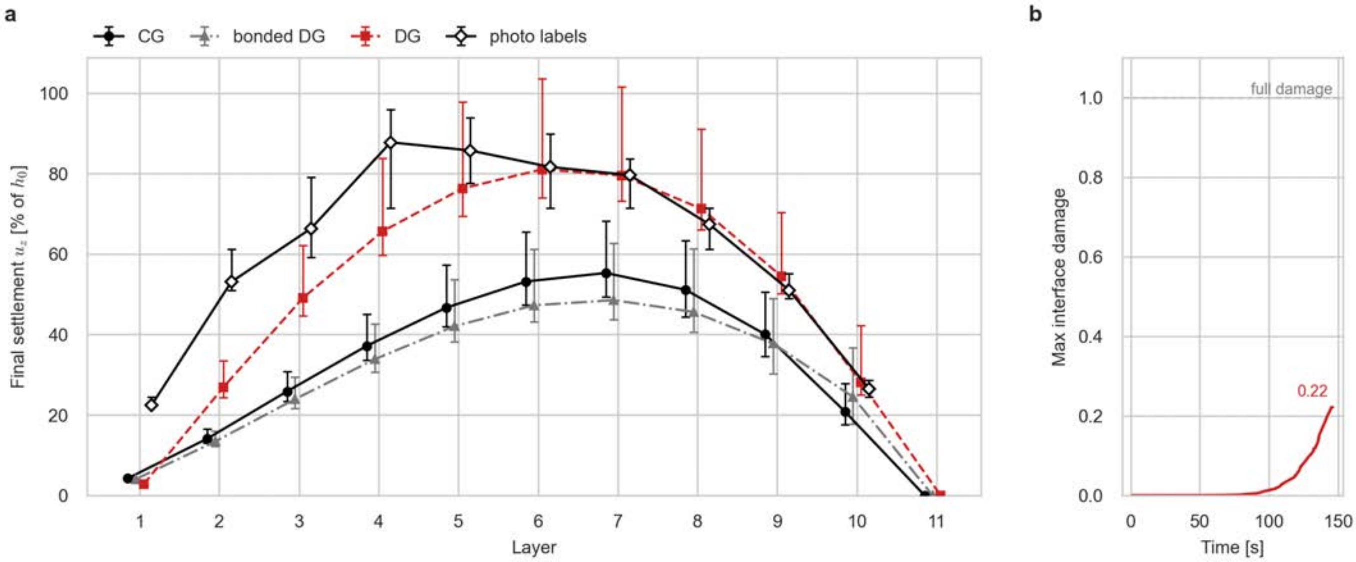

Figure 15: Per-layer settlement of the cylinder for the three formulations. (a) Final per-layer settlement, each layer referenced to its coverage instant, in percent of one layer height, for the continuous Galerkin baseline, the bonded-DG control, and the cohesive DG model, alongside the direct image-based measurement (open markers). Every series gives the median with interquartile error bars, the three simulations over their azimuthal samples and the measurement over image columns; the first three measured layers (partly occluded at start-up) are less reliable. The cohesive DG settlement recovers the measured profile while the two perfectly bonded formulations underpredict it, and the near coincidence of the CG and bonded-DG curves shows the additional settlement is an interface effect rather than a discretization effect. (b) Maximum inter-layer cohesive damage in the DG run, the diagnostic the bonded formulations cannot provide; the bonds stay far from full damage and no interface opens.

The interface diagnostic is paid for in computational cost (Figure 16), and the bonded-DG control again separates its two sources. On the same mesh both DG formulations carry 3.7 times the degrees of freedom of the CG run. Moving from CG to the control, which adds the discontinuous discretization and its interior-facet assembly while leaving the interfaces bonded, raises the wall-clock from 44.6 s to 99.5 s, a factor of 2.2, with the Newton count unchanged at 170: the viscoplastic update is explicit, so the displacement solve is linear at fixed state and both systems remain affine. Activating the cohesive law then raises it to 598 s, a further factor of 6.0, as the nonlinear interface drives the iteration count to 1 306. The cost composition shifts in step: the implicit solve accounts for 22 % of the CG wall-clock, 67 % of the bonded-DG wall-clock, and 94 % of the cohesive-DG wall-clock (564 s of 598 s), while the explicit Perzyna update (32 s to 34 s) is common to all three. The CG baseline is therefore the economical choice when bulk collapse is known to govern; the DG formulation supplies, at a quantified premium, both the interface diagnostic and the compliance that matches the measured settlement.

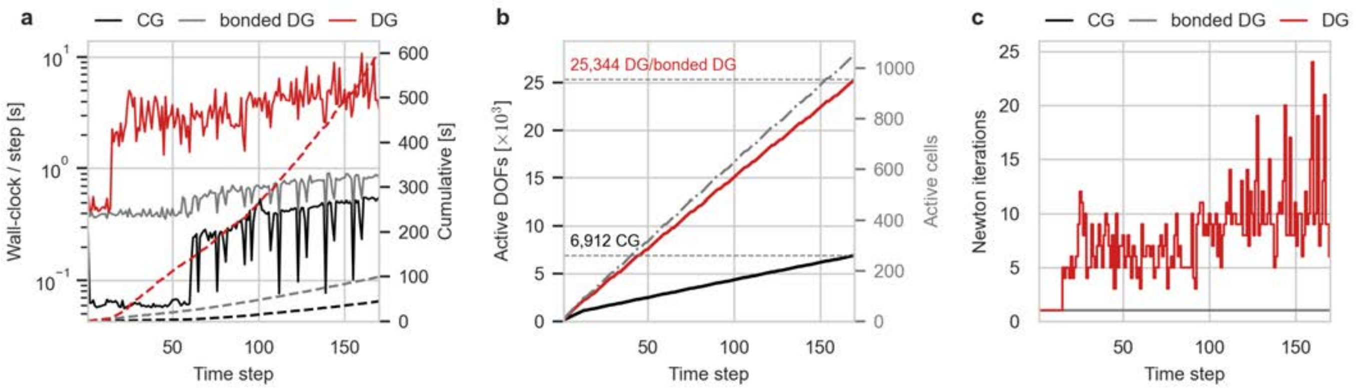

Figure 16: Computational cost of the cylinder simulations for the three formulations (continuous Galerkin, bonded-DG control, and cohesive DG; serial runs over 170 time steps). (a) Wall-clock time per step (solid, left axis, logarithmic) and cumulative (dashed, right axis). (b) Growth of the active displacement degrees of freedom (left axis) and active cells (right axis) as layers are deposited; the three runs share the mesh and activation schedule, and the two DG formulations share the degree-of-freedom count. (c) Newton iterations per step; the CG and bonded-DG systems are affine and converge in one iteration each, whereas the cohesive DG system is nonlinear, and with the direct solver each iteration entails exactly one linear solve.

4.4. Inter-layer delamination of a printed barrel vault

The second case targets inter-layer delamination, the failure mode the cohesive interface formulation is specifically designed to capture. The experiment is a barrel-vault print conducted at the University of Michigan and documented in the authors' companion study on scaffold-free lamination design for 3DCP vaults [41]. The fabrication platform, material system, and measured parameters are those of Sections 4.1 and 4.2; the vault-specific tooling is the custom steel support frame shown in Figure 17, which defines the springing lines and startup zone.

The first ten layers were deposited onto formwork that supported the intrados, after which the print continued to cantilever beyond the supported region. The structure survived four unsupported layers before delaminating at an inter-layer interface and collapsing at approximately layer 14.

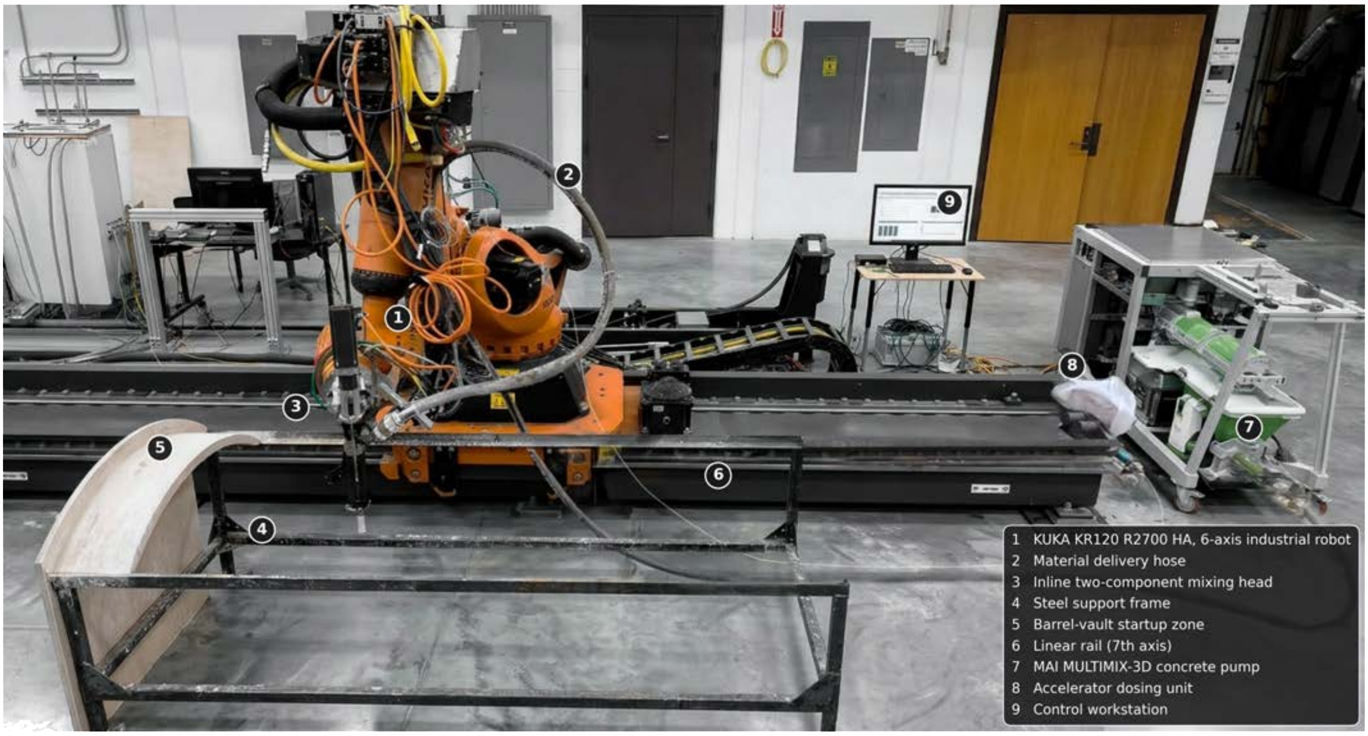

Figure 17: Barrel-vault demonstrator geometry and vault-specific tooling. The steel support frame (4) defines the barrel-vault startup zone (5), from which the cantilevering primary filaments extend. Printing is performed by the KUKA KR120 R2700 HA robot (1) on the linear rail (6); material is delivered through the hose (2) to the inline two-component mixing head (3), supplied by the MAI MULTIMIX-3D pump (7) and accelerator dosing unit (8), controlled from the workstation (9). Span $S = 1200$ mm, rise $h_v = 300$ mm, radius $R = 750$ mm, primary arc $L_p \approx 1391$ mm [41].

The vault is discretized with 150 hexahedral elements along the span, 15 layers along the print direction, and one element through the thickness (2 250 cells total). The intrados of layers 0–10 and the springing faces are clamped through Nitsche boundary conditions; all remaining surfaces are traction-free. Interior facets are split into two categories: intra-layer facets, coupled by symmetric interior-penalty terms, and inter-layer facets, governed by the mixed-mode cohesive traction–separation law with exponential damage. The layer cycle time is $T_\ell \approx 23.2$ s. The material parameters are those of Table 8, and the geometric quantities and density are measured directly [41].

Figure 18 shows that the model reproduces the main progression of the barrel-vault print through failure onset. In particular, it captures the stable supported base, the onset of progressive downward deflection once the print extends beyond the supported region, and delamination at the interface between the supported and cantilevering regions at approximately layer 14, consistent with the experiment. Damage concentrates at this single inter-layer interface while the bulk material remains largely elastic, so the model identifies the governing mechanism as interface delamination, the interface-side counterpart of the bulk-deformation result in Section 4.3. The qualitative differences that become visible in the final post-delamination configuration are expected and reflect idealizations of the present formulation rather than a failure to identify the governing mechanism. First, the equilibrium problem includes gravitational self-weight as the applied load but does not include the mechanical interaction of the nozzle with the printed structure during deposition; such process forces may influence the late-stage separation path. Second, the formulation enforces bonded behavior within each deposited layer through the SIPG intra-layer coupling, while decohesion is permitted only at inter-layer interfaces through the cohesive law, so the model represents inter-layer delamination but not within-layer breakup or tearing. Third, the formulation adopts infinitesimal kinematics and is intended to predict failure onset rather than the subsequent large-displacement collapse. The strongest agreement should therefore be expected up to the onset of delamination, whereas discrepancies in the final separated shape reflect these kinematic and process-level simplifications.

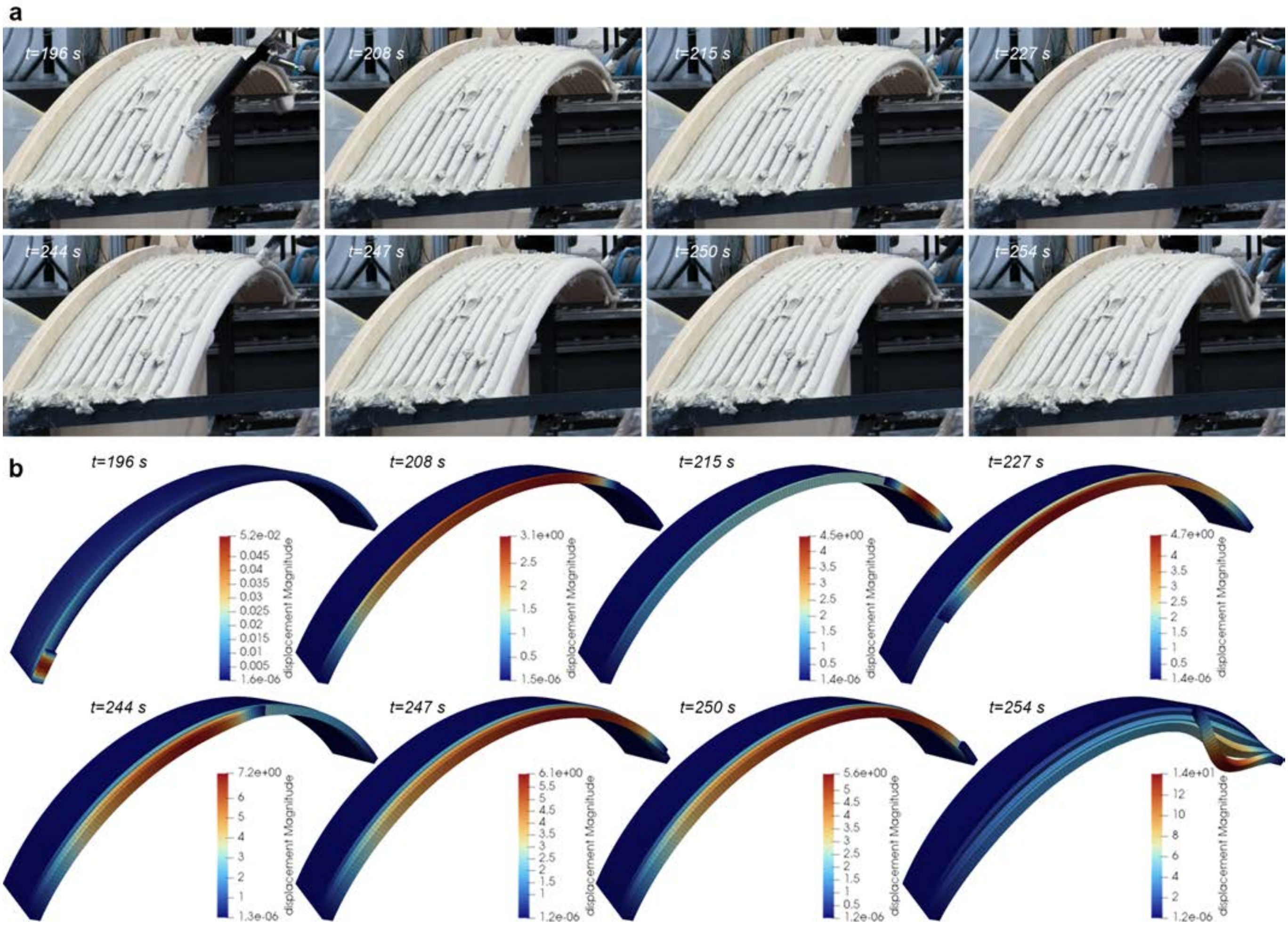

Figure 18: Print progression of the barrel vault. (a) Experimental photographs from [41] showing the supported base, the cantilevering layers with progressive deformation, and delamination at layer 14. (b) Simulated displacement magnitude [mm] at the corresponding stages.

The vault simulation comprised 2 250 cells (all active at failure, 54 000 displacement degrees of freedom) and ran in 147 s on four cores of the hardware described in Section 4.1, over 100 time steps. The implicit displacement solve dominated this cost, accounting for 125.4 s (85% of the time-loop wall-clock), while the explicit Perzyna constitutive update and field output contributed 5.4 s and 1.8 s respectively, with the remaining 14.3 s attributable to MPI communication and assembly overhead. The solver required 210 Newton iterations in total (approximately two per step) and 4 976 aggregate linear (KSP) iterations. Figure 19 reports the per-step and cumulative wall-clock, the growth of the active degrees of freedom as successive layers are deposited, and the per-step solver iteration counts.

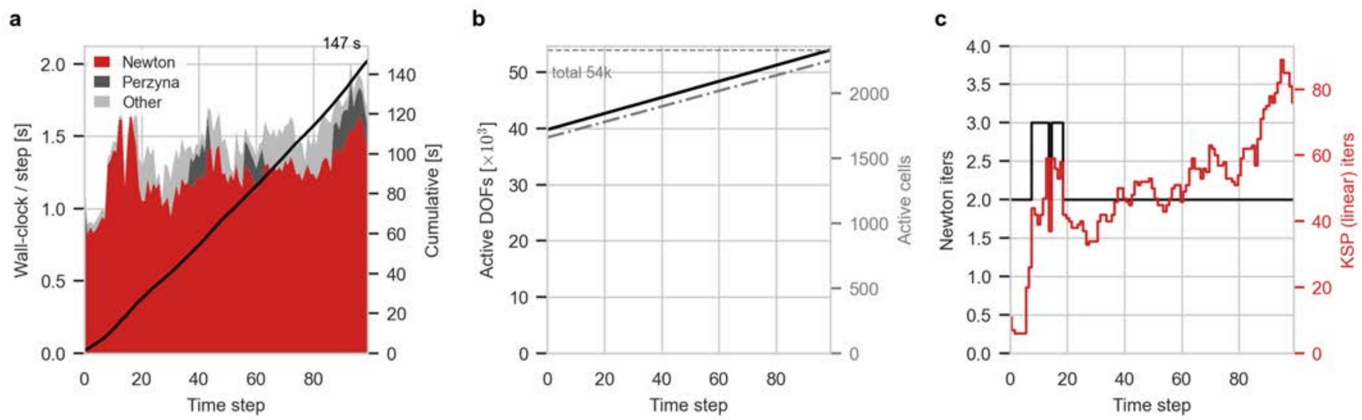

Figure 19: Computational cost of the barrel-vault print simulation. (a) Per-step wall-clock time decomposed into the implicit Newton solve, the explicit Perzyna update, and remaining overhead (left axis), with the cumulative wall-clock superimposed (right axis). (b) Growth of the active displacement degrees of freedom and active cells as layers are activated, approaching the fully-deposited mesh of 2 250 cells and 54 000 DOFs. (c) Newton (nonlinear) and KSP (linear) solver iterations per time step. Timings are for a four-core run over 100 time steps.

5. Conclusions and Discussion

This paper presented a discontinuous Galerkin finite element framework for simulating buildability in 3D concrete printing. The dual interface treatment, symmetric interior penalty coupling within layers and mixed-mode cohesive damage between layers, represents both bulk plastic collapse and interlayer delamination within a single variational form, without crack insertion, remeshing, or enrichment.

The constitutive framework couples three time-dependent mechanisms: an elasto-viscoplastic bulk model with a von Mises yield surface and Perzyna regularization, where all mechanical properties evolve with concrete age through a small set of rheological inputs; a cohesive interface law with a bond quality parameter that captures the dependence of interlayer adhesion on the rest time between successive depositions; and element activation via a smooth birth function that represents the progressive growth of the printed domain without modifying the mesh or the system size.

The implementation was verified through six tests of increasing complexity: a patch test confirming machine-precision reproduction of uniform stress states across both interface types; the method of manufactured solutions establishing optimal spatial convergence rates of $O(h^2)$ in the L^2 norm and $O(h)$ in the broken H^1 semi-norm; machine-precision verification of the cohesive traction–separation law in pure mode I and mixed-mode loading; first-order temporal convergence of the Perzyna integrator with bounded error under adaptive substepping; a self-weight elastic column verifying the coupled system and the activation mechanism against a closed-form solution; and a coupled cohesive equilibrium benchmark reproducing the analytical force–displacement response through peak load, softening, and the residual branch.

Two validation cases, printed on the same robotic platform with different deposition heads and feedstocks, exercised the two failure modes. The first was a cylinder printed from a weak, unaccelerated mortar along a non-planar toolpath and simulated on a toolpath-conformal mesh; its interfaces remained in compression and the print failed by plastic collapse of the bulk. The DG formulation and the CG baseline, obtained from the same variational form on the continuous subspace of the broken space, both reproduced the recorded progression. The cohesive DG settlement tracked the measured profile to within roughly 4 % of a layer height over the mid-to-upper stack, peaking near 81 % against a measured 80 % to 88 %, whereas the CG baseline and a bonded-DG control, which shares the discontinuous discretization but ties the inter-layer facets, both underpredicted the measurement. Because these two perfectly bonded profiles nearly coincide, the additional settlement that brings the DG prediction into agreement with the measurement is a compliance of the cohesive interfaces rather than an effect of the discretization. The DG run further reproduced the confinement of the first layer and its progressive covering by the layer above, a feature the continuity of the CG space precludes, and its interface diagnostic, available only in the cohesive run, showed damage below 0.23 and no opening, identifying bulk yielding as the governing mechanism. The same three-way comparison quantified the price of the interface treatment: both DG formulations carry 3.7 times the degrees of freedom of the CG baseline, and activating the cohesive law raises the wall-clock to a factor of 13 over CG, the bonded-DG control isolating the discretization cost (a factor of 2.2) from the interface cost (a further factor of 6.0). The CG discretization remains the economical choice when bulk collapse is known in advance to govern, and the DG premium purchases the diagnostic that makes such advance knowledge unnecessary.

The second case, the inter-layer delamination of a printed barrel vault drawn from the authors' companion experimental study [41], matched the observed failure layer and deformation sequence, with damage concentrating at the interface between the supported and cantilevered regions while the bulk remained largely elastic. Together, the two cases demonstrate that the dual interface treatment activates the correct failure mode without user intervention: the formulation does not presuppose whether plastic collapse or delamination will govern. The primary value of the framework at its current stage of validation is this failure-mode discrimination; quantitative prediction of deformation magnitudes remains dependent on constitutive calibration, particularly the relationship between laboratory-measured and as-printed material properties.

Several limitations should be noted. The formulation adopts a small-strain kinematic assumption, which precludes elastic buckling, a geometric instability that requires the geometric stiffness arising only in a finite-deformation framework; the present formulation therefore captures the onset of plastic collapse and delamination but not bifurcation-type buckling. Extending the framework to buckling requires replacing the linear strain measure with a finite-deformation counterpart (e.g., a Green–Lagrange strain with the corresponding geometric stiffness term); the DG interface treatment, cohesive law, and element activation machinery carry over without modification. The computational cost of the DG discretization is substantially higher than that of an equivalent continuous Galerkin model, as quantified in Section 4.3, because each element carries independent degrees of freedom and the interface terms add coupling and nonlinearity. The von Mises yield criterion does not capture pressure-sensitive behavior that may become relevant under high confinement or in geometries where hydrostatic stress is significant; a Drucker–Prager or similar criterion requires only substitution of the yield function and flow direction, with no changes to the DG formulation or the solution algorithm. The bond quality model assumes interlayer adhesion is governed by a single dimensionless parameter frozen at the moment of contact, neglecting subsequent mechanisms such as moisture transport, thermal effects, and continued chemical bonding across the interface. Finally, the two validation cases each exercise one failure mode in isolation; geometries in which plastic collapse and delamination interact or trigger one another remain to be investigated.

The framework opens several directions for future work. The most immediate extension is a finite-deformation formulation that adds elastic buckling as a third failure mode alongside plastic collapse and delamination, completing the set of mechanisms relevant to 3DCP buildability. Coupling the buildability simulation with robotic motion planning would enable assessment of print-path feasibility during trajectory generation rather than as a post hoc check. Incorporating a pressure-dependent yield criterion and a more detailed interlayer bonding model informed by microstructural measurements would improve fidelity across materials and printing conditions. Finally, the element activation and cohesive interface machinery are not specific to concrete; the same framework applies to other additive manufacturing processes in which layer adhesion and time-dependent material behavior govern structural integrity during fabrication.

CRediT Authorship Contribution Statement

Abdallah Kamhawi: Conceptualization; Data curation; Formal analysis; Investigation; Methodology; Project administration; Resources; Software; Validation; Visualization; Writing – original draft; Writing – review & editing.

Mania Aghaei Meibodi: Conceptualization; Data curation; Formal analysis; Investigation; Methodology; Project administration; Resources; Validation; Writing – review & editing.

Jesse Capecelatro: Conceptualization; Investigation; Methodology; Project administration; Resources; Writing – review & editing.

Declaration of Competing Interest

The authors declare that they have no known competing financial interests or personal relationships that could have appeared to influence the work reported in this paper.

Data Availability

The experimental data, input parameters, and computational scripts supporting the findings of this study are openly available at https://github.com/Kamhawi/3dcp-fea.

References

[1] F. Hamidi, F. Aslani, Additive manufacturing of cementitious composites: Materials, methods, potentials, and challenges, Construction and Building Materials 218 (2019) 582–609. doi:10.1016/j.conbuildmat.2019.05.140.

[2] V. N. Nerella, S. Hempel, V. Mechtcherine, Effects of layer-interface properties on mechanical performance of concrete elements produced by extrusion-based 3D-printing, Construction and Building Materials 205 (2019) 586–601. doi:10.1016/j.conbuildmat.2019.01.235.

[3] R. A. Buswell, W. R. Leal de Silva, S. Z. Jones, J. Dirrenberger, 3D printing using concrete extrusion: A roadmap for research, Cement and Concrete Research 112 (2018) 37–49. doi:10.1016/j.cemconres.2018.05.006.

[4] A. Kamhawi, M. A. Meibodi, Techniques and strategies in extrusion based 3D concrete printing of complex components to prevent premature failure, Automation in Construction 168 (2024) 105768. doi:10.1016/j.autcon.2024.105768.

[5] A. Kamhawi, J. Brown, A. Fahmy, M. Aghaei Meibodi, Waste-free production of ultra-thin concrete panels via robotic 3D printing and CNC dynamic bed device, in: RILEM International Conference on Concrete and Digital Fabrication, Springer, 2024, pp. 99–106. doi:10.1007/978-3-031-70031-6_11.

[6] M. Aghaei Meibodi, A. Kamhawi, A. Foroughi Dehnavi, Y. Li, Non-planar slicing for high-genus surfaces with non-coplanar interfaces, Virtual and Physical Prototyping 21 (1) (2026) e2603853. doi:10.1080/17452759.2025.2603853.

[7] A. Kamhawi, Y. Lin, C. Watson, K. Barton, M. A. Meibodi, A framework for process anomaly detection in 3D concrete printing, Additive Manufacturing (2025) 105056doi:10.1016/j.addma.2025.105056.

[8] M. A. Meibodi, Y. Lin, H. Chen, Hybrid approaches towards 3D concrete printing for lightweight reinforced concrete structures, in: Digital Concrete 2024 – Supplementary Proceedings, 2024.

[9] Y. Lin, A. Bayramvand, M. Aghaei Meibodi, Towards lightweight structure: Coupling topology optimization with non-planar 3D concrete printing, in: The International Conference on Computational Design and Robotic Fabrication, Springer, 2024, pp. 3–12. doi:10.1007/978-981-99-8405-3_1.

[10] Y. Lin, A. Bayramvand, M. A. Meibodi, Branch wall: Developing topology informed non-planar toolpath and variable deposition rate for 3D concrete printing of topology optimized load bearing wall, SSRN Electronic Journal (2023). doi:10.2139/ssrn.4663173.

[11] R. Wolfs, D. Bos, J.-F. Caron, M. Gerke, R. Mesnil, R. Buswell, N. Ducoulombier, N. Hack, E. Keita, P. Kinnell, K. Mawas, V. Mechtcherine, L. Miranda, D. Sokolov, J. Versteege, N. Roussel, On-line and in-line quality assessment across all scale levels of 3D concrete printing, Cement and Concrete Research 185 (2024) 107646. doi:10.1016/j.cemconres.2024.107646.

[12] F. Bos, R. Wolfs, Z. Ahmed, T. Salet, Large scale testing of digitally fabricated concrete (dfc) elements, in: First RILEM International Conference on Concrete and Digital Fabrication, Vol. 19, Springer, 2018, pp. 129–147. doi:10.1007/978-3-319-99519-9_12.

[13] R. Wolfs, F. Bos, T. Salet, Early age mechanical behaviour of 3d printed concrete: Numerical modelling and experimental testing, Cement and Concrete Research 106 (2018) 103–116. doi:10.1016/j.cemconres.2018.02.001.

[14] A. Suiker, Mechanical performance of wall structures in 3d printing processes: Theory, design tools and experiments, International Journal of Mechanical Sciences 137 (2018) 145–170. doi:10.1016/j.ijmecsci.2018.01.010.

[15] G. Rizzieri, D. Bos, R. Wolfs, L. Ferrara, M. Cremonesi, A unified fluid-solid elasto-viscoplastic finite element model for the simulation of 3d concrete printing across process scales, Computer Methods in Applied Mechanics and Engineering 457 (2026) 118929–. doi:10.1016/j.cma.2026.118929.

[16] J. Reinold, K. Daadouch, G. Meschke, Numerical simulation of three dimensional concrete printing based on a unified fluid and solid mechanics formulation, Frontiers of Structural and Civil Engineering 18 (4) (2024) 491–515. doi:10.1007/s11709-024-1082-2.

[17] T. Ooms, G. Vantyghem, R. Van Coile, W. De Corte, A parametric modelling strategy for the numerical simulation of 3D concrete printing with complex geometries, Additive Manufacturing 38 (2021) 101743. doi:10.1016/j.addma.2020.101743.

[18] N. Roussel, J. Spangenberg, J. Wallevik, R. Wolfs, Numerical simulations of concrete processing: From standard formative casting to additive manufacturing, Cement and Concrete Research 135 (2020) 106075. doi:10.1016/j.cemconres.2020.106075.

[19] R. Comminal, W. R. Leal da Silva, T. J. Andersen, H. Stang, J. Spangenberg, Modelling of 3D concrete printing based on computational fluid dynamics, Cement and Concrete Research 138 (2020) 106256. doi:10.1016/j.cemconres.2020.106256.

[20] J. Reinold, V. N. Nerella, V. Mechtcherine, G. Meschke, Extrusion process simulation and layer shape prediction during 3d-concrete-printing using the particle finite element method, Automation in Construction 136 (2022) 104173. doi:10.1016/j.autcon.2022.104173.

[21] R. Wolfs, T. Salet, N. Roussel, Filament geometry control in extrusion-based additive manufacturing of concrete: The good, the bad and the ugly, Cement and Concrete Research 150 (2021) 106615. doi:10.1016/j.cemconres.2021.106615.

[22] G. Rizzieri, L. Ferrara, M. Cremonesi, Numerical simulation of the extrusion and layer deposition processes in 3d concrete printing with the particle finite element method, Computational Mechanics 73 (2) (2024) 277–295. doi:10.1007/s00466-023-02367-y.

[23] N. Roussel, Rheological requirements for printable concretes, Cement and Concrete Research 112 (2018) 76–85. doi:10.1016/j.cemconres.2018.04.005.

[24] J. Kruger, S. Zeranka, G. van Zijl, 3D concrete printing: A lower bound analytical model for buildability performance quantification, Automation in Construction 106 (2019) 102904. doi:10.1016/j.autcon.2019.102904.

[25] R. J. M. Wolfs, A. S. J. Suiker, Structural failure during extrusion-based 3d printing processes, The International Journal of Advanced Manufacturing Technology 104 (1–4) (2019) 565–584. doi:10.1007/s00170-019-03844-6.

[26] A. Suiker, R. Wolfs, S. Lucas, T. Salet, Elastic buckling and plastic collapse during 3d concrete printing, Cement and Concrete Research 135 (2020) 106016. doi:10.1016/j.cemconres.2020.106016.

[27] A. Perrot, D. Rangeard, A. Pierre, Structural built-up of cement-based materials used for 3d-printing extrusion techniques, Materials and Structures 49 (4) (2016) 1213–1220. doi:10.1617/s11527-015-0571-0.

[28] R. Jayathilakage, P. Rajeev, J. Sanjayan, Yield stress criteria to assess the buildability of 3d concrete printing, Construction and Building Materials 240 (2020) 117989. doi:10.1016/j.conbuildmat.2019.117989.

[29] H. Liu, T. Ding, J. Xiao, V. Mechtcherine, Buildability prediction of 3d–printed concrete at early-ages: A numerical study with drucker–prager model, Additive Manufacturing 55 (2022) 102821. doi:10.1016/j.addma.2022.102821.

[30] J. Kruger, S. Zeranka, G. van Zijl, An ab initio approach for thixotropy characterisation of (nanoparticle-infused) 3D printable concrete, Construction and Building Materials 224 (2019) 372–386. doi:10.1016/j.conbuildmat.2019.07.078.

[31] J. Kruger, S. Zeranka, G. van Zijl, A rheology-based quasi-static shape retention model for digitally fabricated concrete, Construction and Building Materials 254 (2020) 119241. doi:10.1016/j.conbuildmat.2020.119241.

[32] N. Roussel, A thixotropy model for fresh fluid concretes: Theory, validation and applications, Cement and Concrete Research 36 (10) (2006) 1797–1806. doi:10.1016/j.cemconres.2006.05.025.

[33] N. Roussel, G. Ovarlez, S. Garrault, C. Brumaud, The origins of thixotropy of fresh cement pastes, Cement and Concrete Research 42 (1) (2012) 148–157. doi:10.1016/j.cemconres.2011.09.004.

[34] T. Lecompte, A. Perrot, Non-linear modeling of yield stress increase due to scc structural build-up at rest, Cement and Concrete Research 92 (2017) 92–97. doi:10.1016/j.cemconres.2016.11.020.

[35] E. Keita, H. Bessaies-Bey, W. Zuo, P. Belin, N. Roussel, Weak bond strength between successive layers in extrusion-based additive manufacturing: measurement and physical origin, Cement and Concrete Research 123 (2019) 105787. doi:10.1016/j.cemconres.2019.105787.

[36] J. G. Sanjayan, B. Nematollahi, M. Xia, T. Marchment, Effect of surface moisture on inter-layer strength of 3d printed concrete, Construction and Building Materials 172 (2018) 468–475. doi:10.1016/j.conbuildmat.2018.03.232.

[37] G. M. Moelich, J. Kruger, R. Combrinck, Modelling the interlayer bond strength of 3d printed concrete with surface moisture, Cement and Concrete Research 150 (2021) 106559. doi:10.1016/j.cemconres.2021.106559.

[38] D. Lowke, A. Anton, R. Buswell, S. E. Jenny, R. J. Flatt, E. L. Fritschi, N. Hack, I. Mai, M. Popescu, H. Kloft, Digital fabrication with concrete beyond horizontal planar layers, Cement and Concrete Research 186 (2024) 107663. doi:10.1016/j.cemconres.2024.107663.

[39] P. Carneau, R. Mesnil, N. Roussel, O. Baverel, Additive manufacturing of cantilever - from masonry to concrete 3d printing, Automation in Construction 116 (2020) 103184. doi:10.1016/j.autcon.2020.103184.

[40] S. Li, H. Nguyen-Xuan, P. Tran, Digital design and parametric study of 3d concrete printing on non-planar surfaces, Automation in Construction 145 (2023) 104624. doi:10.1016/j.autcon.2022.104624.

[41] A. Kamhawi, M. Aghaei Meibodi, Cohesive vault: Scaffold-free 3d concrete printing of vaulted structures via zig-zag lamination, manuscript under review at Virtual and Physical Prototyping (2026).

[42] J. Kruger, G. van Zijl, A compendious review on lack-of-fusion in digital concrete fabrication, Additive Manufacturing 37 (2021) 101654. doi:10.1016/j.addma.2020.101654.

[43] D. N. Arnold, F. Brezzi, B. Cockburn, L. D. Marini, Unified analysis of discontinuous galerkin methods for elliptic problems, SIAM Journal on Numerical Analysis 39 (5) (2002) 1749–1779. doi:10.1137/S0036142901384162.

[44] L. Noels, R. Radovitzky, A general discontinuous galerkin method for finite hyperelasticity. formulation and numerical applications, International Journal for Numerical Methods in Engineering 68 (1) (2006) 64–97. doi:10.1002/nme.1699.

[45] R. Radovitzky, A. Seagraves, M. Tupek, L. Noels, A scalable 3d fracture and fragmentation algorithm based on a hybrid, discontinuous galerkin, cohesive element method, Computer Methods in Applied Mechanics and Engineering 200 (1–4) (2011) 326–344. doi:10.1016/j.cma.2010.08.014.

[46] V. P. Nguyen, Discontinuous galerkin/extrinsic cohesive zone modeling: Implementation caveats and applications in computational fracture mechanics, Engineering Fracture Mechanics 128 (2014) 37–68. doi:10.1016/j.engfracmech.2014.07.003.

[47] P. Hansbo, K. Salomonsson, A discontinuous galerkin method for cohesive zone modelling, Finite Elements in Analysis and Design 102–103 (2015) 1–6. doi:10.1016/j.finel.2015.04.008.

[48] L. Noels, R. Radovitzky, An explicit discontinuous galerkin method for non-linear solid dynamics: Formulation, parallel implementation and scalability properties, International Journal for Numerical Methods in Engineering 74 (9) (2008) 1393–1420. doi:10.1002/nme.2213.

[49] S. Levy, J. F. Molinari, R. Radovitzky, Dynamic fragmentation of a brittle plate under biaxial loading: strength or toughness controlled?, International Journal of Fracture 174 (2) (2012) 203–215. doi:10.1007/s10704-012-9691-5.

[50] J. Huang, C. Feng, X. Wang, Y. Zhang, Continuous–discontinuous element method for simulating three-dimensional reinforced concrete structures, Structural Concrete 26 (5) (2025) 5846–5861. arXiv:https://onlinelibrary.wiley.com/doi/pdf/10.1002/suco.202300531, doi:https://doi.org/10.1002/suco.202300531.
URL https://onlinelibrary.wiley.com/doi/abs/10.1002/suco.202300531

[51] J. Mergheim, E. Kuhl, P. Steinmann, A hybrid discontinuous galerkin/interface method for the computational modelling of failure, Communications in Numerical Methods in Engineering 20 (7) (2004) 511–519. doi:10.1002/cnm.689.

[52] G. N. Wells, L. J. Sluys, A new method for modelling cohesive cracks using finite elements, International Journal for Numerical Methods in Engineering 50 (12) (2001) 2667–2682. doi:10.1002/nme.143.

[53] R. Wolfs, F. Bos, T. Salet, Triaxial compression testing on early age concrete for numerical analysis of 3d concrete printing, Cement and Concrete Composites 104 (2019) 103344. doi:10.1016/j.cemconcomp.2019.103344.

[54] A. Alexandridis, N. Gardner, Mechanical behaviour of fresh concrete, Cement and Concrete Research 11 (3) (1981) 323–339. doi:10.1016/0008-8846(81)90105-8.

[55] D. C. Drucker, W. Prager, Soil mechanics and plastic analysis or limit design, Quarterly of Applied Mathematics 10 (2) (1952) 157–165. doi:10.1090/qam/48291.

[56] P. P. Camanho, C. G. Dávila, M. F. de Moura, Numerical simulation of mixed-mode progressive delamination in composite materials, Journal of Composite Materials 37 (16) (2003) 1415–1438. doi:10.1177/0021998303034505.

[57] M. Benzeggagh, M. Kenane, Measurement of mixed-mode delamination fracture toughness of unidirectional glass/epoxy composites with mixed-mode bending apparatus, Composites Science and Technology 56 (4) (1996) 439–449. doi:10.1016/0266-3538(96)00005-X.

[58] K. Park, G. H. Paulino, J. R. Roesler, A unified potential-based cohesive model of mixed-mode fracture, Journal of the Mechanics and Physics of Solids 57 (6) (2009) 891–908. doi:10.1016/j.jmps.2008.10.003.

[59] D. R. Smith, An Introduction to Continuum Mechanics - after Truesdell and Noll, 1st Edition, Vol. 22 of Solid Mechanics and Its Applications, Springer, Dordrecht, 1993. doi:10.1007/978-94-017-0713-8.

[60] W. Macke, L. I. Sedov, Introduction to the Mechanics of a Continuous Medium. (Adiwes International Series in the Engineering Sciences). XVI + 270 S. m. 11 Fig. Reading, Mass./Palo Alto/London 1965. Addison-Wesley Publishing Company, Inc. Preis geb. $12.50, Zeitschrift für Angewandte Mathematik und Mechanik 45 (5) (1965) 369. doi:10.1002/zamm.19650450535.

[61] G. A. Holzapfel, Nonlinear solid mechanics: A continuum approach for engineering science, Meccanica 37 (4–5) (2002) 489–490. doi:10.1023/A:1020843529530.

[62] I. A. Baratta, J. P. Dean, J. S. Dokken, M. Habera, J. S. Hale, C. N. Richardson, M. E. Rognes, M. W. Scroggs, N. Sime, G. N. Wells, DOLFINx: the next generation FEniCS problem solving environment, preprint (2023). doi:10.5281/zenodo.10447666.

[63] M. S. Alnaes, A. Logg, K. B. Ølgaard, M. E. Rognes, G. N. Wells, Unified form language: A domain-specific language for weak formulations of partial differential equations, ACM Transactions on Mathematical Software 40 (2014). doi:10.1145/2566630.

[64] M. W. Scroggs, I. A. Baratta, C. N. Richardson, G. N. Wells, Basix: a runtime finite element basis evaluation library, Journal of Open Source Software 7 (73) (2022) 3982. doi:10.21105/joss.03982.

[65] S. Balay, S. Abhyankar, M. F. Adams, J. Brown, P. Brune, K. Buschelman, L. Dalcin, A. Dener, V. Eijkhout, W. D. Gropp, H. Isaacs, P. Jolivet, D. Karpeev, D. Kaushik, M. G. Knepley, F. Kong, S. Kruger, D. A. May, L. C. McInnes, R. T. Mills, L. Mitchell, T. Munson, J. E. Roman, K. Rupp, P. Sanan, J. Sarich, B. F. Smith, S. Zampini, H. Zhang, J. Zhang, PETSc/TAO users manual, Tech. Rep. ANL-21/39 – Revision 3.21, Argonne National Laboratory (2024). doi:10.2172/2205494.

[66] Y. Saad, M. H. Schultz, GMRES: A generalized minimal residual algorithm for solving nonsymmetric linear systems, SIAM Journal on Scientific and Statistical Computing 7 (3) (1986) 856–869. doi:10.1137/0907058.

[67] P. R. Amestoy, I. S. Duff, J. Koster, J.-Y. L'Excellent, A fully asynchronous multifrontal solver using distributed dynamic scheduling, SIAM Journal on Matrix Analysis and Applications 23 (1) (2001) 15–41. doi:10.1137/S0895479899358194.

[68] C. Geuzaine, J.-F. Remacle, Gmsh: A 3-D finite element mesh generator with built-in pre- and post-processing facilities, International Journal for Numerical Methods in Engineering 79 (11) (2009) 1309–1331. doi:10.1002/nme.2579.

[69] D. N. Arnold, An interior penalty finite element method with discontinuous elements, SIAM Journal on Numerical Analysis 19 (4) (1982) 742–760. doi:10.1137/0719052.

[70] P. Michaleris, Modeling metal deposition in heat transfer analyses of additive manufacturing processes, Finite Elements in Analysis and Design 86 (2014) 51–60. doi:10.1016/j.finel.2014.04.003.

[71] J. Reinold, G. Meschke, Algorithm for aging materials with evolving stiffness based on a multiplicative split, Computer Methods in Applied Mechanics and Engineering 397 (2022) 115080. doi:10.1016/j.cma.2022.115080.

[72] N. Roussel, Steady and transient flow behaviour of fresh cement pastes, Cement and Concrete Research 35 (9) (2005) 1656–1664. doi:10.1016/j.cemconres.2004.08.001.

[73] V. Mechtcherine, F. P. Bos, A. Perrot, W. R. Leal da Silva, V. N. Nerella, S. Fataei, R. J. M. Wolfs, M. Sonebi, N. Roussel, Extrusion-based additive manufacturing with cement-based materials – production steps, processes, and their underlying physics: A review, Cement and Concrete Research 132 (2020) 106037. doi:10.1016/j.cemconres.2020.106037.

[74] D. Lootens, P. Jousset, L. Martinie, N. Roussel, R. J. Flatt, Yield stress during setting of cement pastes from penetration tests, Cement and Concrete Research 39 (5) (2009) 401–408. doi:10.1016/j.cemconres.2009.01.012.

[75] F. Mahaut, S. Mokéddem, X. Chateau, N. Roussel, G. Ovarlez, Effect of coarse particle volume fraction on the yield stress and thixotropy of cementitious materials, Cement and Concrete Research 38 (11) (2008) 1276–1285. doi:10.1016/j.cemconres.2008.06.001.

[76] D. Feys, R. Verhoeven, G. De Schutter, Fresh self compacting concrete, a shear thickening material, Cement and Concrete Research 38 (7) (2008) 920–929. doi:10.1016/j.cemconres.2008.02.008.

[77] T. Voigt, G. Ye, Z. Sun, S. P. Shah, Comparison of ultrasonic wave transmission and reflection measurements with P- and S-waves on early age mortar and concrete, Materials and Structures 38 (2005) 729–738. doi:10.1007/BF02479285.

[78] ASTM International, Standard test methods for time of setting of hydraulic cement by Vicat needle, ASTM C191-21 (2021). doi:10.1520/C0191-21.

[79] E. Brühwiler, F. H. Wittmann, The wedge splitting test, a new method of performing stable fracture mechanics tests, Engineering Fracture Mechanics 35 (1–3) (1990) 117–125. doi:10.1016/0013-7944(90)90189-N.

[80] A. Logg, K.-A. Mardal, G. N. Wells, et al., Automated Solution of Differential Equations by the Finite Element Method, Springer, 2012. doi:10.1007/978-3-642-23099-8.

[81] P. Perzyna, Fundamental problems in viscoplasticity, in: Advances in Applied Mechanics, Vol. 9, Elsevier, 1966, pp. 243–377. doi:10.1016/S0065-2156(08)70009-7.

[82] R. von Mises, Mechanik der festen Körper im plastisch-deformablen Zustand, Nachrichten von der Gesellschaft der Wissenschaften zu Göttingen, Mathematisch-Physikalische Klasse (1913) 582–592.

[83] E. C. Bingham, Fluidity and plasticity, by Eugene C. Bingham, McGraw-Hill Book Company, Inc., 1922.

[84] M. Kojic, K.-J. Bathe, Inelastic analysis of solids and structures, 1st Edition, Springer, 2005. doi:10.1007/b137717.

[85] I. Cormeau, Numerical stability in quasi-static elasto/visco-plasticity, International Journal for Numerical Methods in Engineering 9 (1) (1975) 109–127. doi:10.1002/nme.1620090110.

[86] T. J. Coogan, D. O. Kazmer, Modeling of interlayer contact and contact pressure during fused filament fabrication, Journal of Rheology 63 (4) (2019) 655–672. doi:10.1122/1.5093033.

[87] S. K. Kim, D. O. Kazmer, A. R. Colon, T. J. Coogan, A. M. Peterson, Non-newtonian modeling of contact pressure in fused filament fabrication, Journal of Rheology 65 (1) (2021) 27–42. doi:10.1122/8.0000052.

[88] S. A. O. Nair, S. Panda, A. Tripathi, N. Neithalath, Relating print velocity and extrusion characteristics of 3d-printable cementitious binders: Implications towards testing methods, Additive Manufacturing 46 (2021) 102127. doi:10.1016/j.addma.2021.102127.

[89] X.-P. Xu, A. Needleman, Numerical simulations of fast crack growth in brittle solids, Journal of the Mechanics and Physics of Solids 42 (9) (1994) 1397–1434. doi:10.1016/0022-5096(94)90003-5.

[90] A. Needleman, An analysis of tensile decohesion along an interface, Journal of the Mechanics and Physics of Solids 38 (3) (1990) 289–324. doi:10.1016/0022-5096(90)90001-K.

[91] J. Nitsche, Über ein variationsprinzip zur lösung von dirichlet-problemen bei verwendung von teilräumen, die keinen randbedingungen unterworfen sind, Abhandlungen aus dem Mathematischen Seminar der Universität Hamburg 36 (1) (1971) 9–15. doi:10.1007/BF02995904.

[92] L. Armijo, Minimization of functions having lipschitz continuous first partial derivatives, Pacific Journal of Mathematics 16 (1) (1966) 1–3. doi:10.2140/pjm.1966.16.1.

[93] B. M. Irons, A. Razzaque, Experience with the patch test for convergence of finite elements, in: The Mathematical Foundations of the Finite Element Method with Applications to Partial Differential Equations, Academic Press, 1972, pp. 557–587. doi:10.1016/B978-0-12-068650-6.50025-3.

[94] R. L. Taylor, J. C. Simo, O. C. Zienkiewicz, A. C. H. Chan, The patch test-a condition for assessing fem convergence, International Journal for Numerical Methods in Engineering 22 (1) (1986) 39–62. doi:10.1002/nme.1620220105.

[95] P. J. Roache, Code verification by the method of manufactured solutions, Journal of Fluids Engineering 124 (1) (2002) 4–10. doi:10.1115/1.1436090.

[96] J. G. M. Van Mier, Fracture Processes of Concrete, CRC Press, 1996. doi:10.1201/b22384.